CHALMERS
UNIVERSITY OF TECHNOLOGY

Measurements of Air Ion Concentrations and Electric Field Strengths for HVDC Applications

Master's thesis in Electric Power Engineering

ANDERS MIKIVER

Department of Materials and Manufacturing Technology
CHALMERS UNIVERSITY OF TECHNOLOGY
Gothenburg, Sweden 2017

Master’s thesis

Measurements of Air Ion Concentrations and Electric Field Strengths for HVDC Applications

ANDERS MIKIVER

Department of Materials and Manufacturing Technology
Division of High Voltage Engineering
Chalmers University of Technology
Gothenburg, Sweden 2017

Measurements of Air Ion Concentrations and Electric Field Strengths for HVDC Applications
ANDERS MIKIVER

Supervisor: Ph.D. Joachim Schiessling, ABB Corporate Research
Examiner: Prof. Yuriy Serdyuk, Chalmers University of Technology

Master's Thesis 2017:204
Department of Materials and Manufacturing Technology
Division of High Voltage Engineering
Chalmers University of Technology
SE-412 96 Gothenburg
Telephone +46 31 772 1000

Typeset in LaTeX
Printed by Reproservice
Gothenburg, Sweden 2017

Measurements of Air Ion Concentrations and Electric Field Strengths for HVDC Applications
ANDERS MIKIVER
Department of Materials and Manufacturing Technology
Chalmers University of Technology

Abstract

High Voltage Direct Current (HVDC) enables transfer of electric power over long distances with high efficiency. In order to further increase the efficiency, the voltage levels are increasing. In turn, this means that for the design of both robust and cost effective electric insulation, the importance of understanding specific DC voltage related phenomena also increase.

For this thesis, specific DC voltage phenomena were studied by means of simultaneous measurements of air ion concentrations, DC electric field strength and ion current. The measurements were performed at ABB Corporate Research in Västerås from January to May of 2017, utilizing a data acquisition system denoted the ion box. Measurements both with and without applied voltage were carried out. The measurements without voltage were implemented in order to observe how the equilibrium ion concentrations varied with respect to location, and with other parameters such as humidity. The high voltage measurements were performed with different voltage polarities and electrode configurations, resulting in different electric field distributions. Additionally, the level of humidity was also varied during the high voltage measurements.

The results of the measurements demonstrate that equilibrium ion concentration correlates strongly with concentrations of radon. In turn, the concentrations of both ions and radon were strongly affected by the air ventilation system for the indoor measurements. Furthermore, due to the tendency of radon gas to accumulate indoors, the measured indoor ion concentrations were larger than the ion concentrations outdoors. From the high voltage measurements the different regions of the general current-voltage characteristics for air were observed. The measurements also confirm that positive corona results in the injection of positive ions, whereas negative corona injects negative ions. In turn, the corona injected ions are shown to disrupt the linear relationship between applied DC voltage and DC electric field strength.

Keywords: HVDC, air ions, conductivity of air, DC electric field strength.

Acknowledgements

First of all, I would like to thank my supervisor Ph.D. Joachim Schiessling for his guidance, support and encouragement.

I would also like to thank Prof. Yuriy Serdyuk for being my examiner, and for an interesting discussions regarding my measurement results.

I would also like to thank Assoc. Prof. Anders Nordlund and Prof. Göran Hugo Nyman at the Department of Physics at Chalmers, for patiently answering my many questions regarding ionizing radiation.

This thesis work has been carried out at ABB Corporate Research Center in Västerås. To which I owe thanks for letting me perform this thesis work, and for providing me with accommodation. Many thanks also to all the employees and fellow thesis workers at ABB Corporate Research Center.

Anders Mikiver, Gothenburg, June 2017

Contents

1

Introduction

This chapter describes the background, aim, scope and outline of the thesis.

1.1 Background

In this section the background to the thesis is presented, i.e. how the study of air ions relate to the further developement of HVDC technology.

1.1.1 High Voltage Direct Current

High Voltage Direct Current (HVDC) is a technology for electric power transmission, that enables bulk power transfer over long distances with high efficiency [1]. The efficiency of long distance HVDC transmission is higher in comparison with traditional High Voltage Alternating Current (HVAC) transmission due to, e.g. the lack of reactive power flow and eddy currents [2]. One way to further increase the efficiency of HVDC, is to increase the voltage level even more. Ultra High Voltage Direct Current (UHVDC) denotes HVDC transmission systems operating at voltages of ± 600 kV DC or higher. Currently, the highest voltage level utilized in UHVDC is ± 800 kV, whereas a ± 1,100 kV transmission system is being planned in China [3]. As the voltage level increase, more emphasis must be put on understanding phenomena that are unique for applied DC voltages in comparison with AC voltages, in order to be to able design robust insulation that prevents electrical breakdown. One such phenomena is how air ions and the resulting electric field distribution are affected by DC voltages.

1.1.2 Air as Electrical Insulation

The atmosphere of the Earth, commonly referred to as air, is the most utilized gaseous insulation medium for high voltage applications, e.g. for overhead lines [4]. Air is composed of several different gases such as nitrogen, oxygen, argon, carbon dioxide and several other trace gases, and contains a varying amount of water vapor. The reasons for the widely use of air as insulation are summarized in the following sentence, even though it may appear obvious. Air does not cost anything, is abundant and it is self-restoring, i.e. it will recover its insulating properties after an electric breakdown [4]. Since air at atmospheric conditions is an excellent insulator, it can only conduct very small electric currents at low electric field strengths. In low fields, i.e. strengths below corona inception, the electrical conductivity is enabled due to naturally occurring concentrations of air ions, which constitutes the main charge carriers of air. However, for higher field strengths additional effects e.g. corona discharges and field emissions act as additional sources of ionization, which increases the conductivity of air significantly. If the electric field strength is increased even more beyond the level of corona inception, due to e.g. overvoltages or charge induced fields, it can result in complete electrical breakdown, which changes the characteristics of air from insulator to conductor [5].

1.1.3 Differences Between AC and DC Electric Stress

Depending on whether AC or DC high voltage is applied between electrodes, the resulting electric field distribution, and hence the electric stress can be very different [6]. The main reason for this is the accumulation of charge carriers that form space and surface charges. Although space and surface charges form in both DC and AC fields, they contribute to larger perturbations in DC fields. Applied DC voltages cause the accumulation of charge carriers to form space charges in the presence of conductivity gradients, and surface charges at interfaces between different mediums. In turn, the charge induced fields created by the space and surface charges can distort the externally applied field, and hence significantly alter the electric stress [6].

1.2 Aim

The aim of the thesis is to contribute to the knowledge of how air ion concentrations are affected by different conditions relevant for HVDC applications.

1.3 Scope

For this thesis work air ion concentrations and electric fields are measured and analysed. Experiments both with and without applied DC voltage are performed. Additionally, other parameters such as humidity are also altered during the experiments. The scope of this thesis is limited in the following ways. Experiments leading to complete electric breakdown is not performed, since it most probably would damage the various instruments installed in the ion box. Hence, air ion dynamics during breakdown is not analysed in this thesis work. Furthermore, no measurements of the air ion mobility spectrum are performed, since such a measuring instrument is not included in the ion box. It follows that variations in the air ion mobility distribution due to e.g. changes in levels of humidity, are not analysed either.

1.4 Outline of the Thesis

This thesis work includes several different measurements of air ion concentrations and electric field strengths, performed at ABB Corporate Research in Västerås. Chapter 1 provides an introduction to the thesis, including background, aim and scope. In Chapter 2 theory related to air ions is presented. This theory is later utilized to interpret and analyse the measurement data presented in Chapter 5. In Chapter 3 a device referred to as the ion box is described. The ion box is a data acquisition (DAQ) system developed by ABB Corporate Research, and contains instruments for measuring e.g. air ion concentrations and electric field strengths. In Chapter 4 the different experimental setups utilizing the ion box are presented. Experiments both in high voltage (HV) environments, and without any applied voltage were performed. For the HV experiments, the level of electric field uniformity is varied by means of several different HV electrode configurations. In addition, other parameters, e.g. level of humidity, are also varied during the experiments. Presentation and analysis of measurement data collected with the ion box is provided in Chapter 5, where air ions and electric fields are studied in terms of steady-state values, dynamic behavior, and during corona discharges. Finally, conclusions and suggestions for future work are presented in Chapter 6.

Sustainable development in the context of increasing voltage levels for HVDC transmissions is also considered. Discussions with reference to the ecological, economical, and social dimensions of sustainable development as defined in [7], are presented in Section 6.3. Finally, one ethical aspect that is considered is point number three in the IEEE Code of Ethics [8], that states that one should agree “to be honest and realistic in stating claims or estimates based on available data”. A discussion regarding this ethical aspect is also presented in Section 6.3.

2

Air Ion Physics

In this chapter background theory relevant to the analysis of air ion concentrations is presented.

2.1 Ionization of Air

Ions are atoms, molecules or molecule clusters that have a net electric charge. Through different ionization processes the net electric charge is generated by means of either adding or removing electrons [9]. Thus, positive air ions are naturally produced by different sources of ionization, which e.g. varies depending on the altitude. Negative air ions, on the other hand, are produced by the attachment of electrons to neutral air molecules. For altitudes between ground and up to about 500 m, the most important source of ionization is radioactivity originating from the ground, whereas the second most important source is cosmic radiation [10]. In the following subsection, the radioactivity originating from the ground is further explained. In Table 2.1 some typical ionization rates from different sources of ionization are presented [11]. In the table, the four bottom rows represent radioactivity originating from the ground. As can be deduced from the table, there are large variations in the ionization rates from the same source, which in turn means that the concentration of ions will vary greatly, depending on location. In addition, ions can also be generated by corona discharges, combustion engines, breaking of water droplets, and by strong winds [12]. At higher altitudes, the contribution from radioactivity originating from the ground decrease, whereas from the contribution cosmic radiation increase. At altitudes above 60-70 km the primary sources of ionization are instead radiation originating from the sun, such as X-ray and extreme ultraviolet radiation [13].

Table 2.1: Typical ionization rates from different sources of ionization [11].

Ionization source	**Altitude (for which the rates are accurate)**	**Ionization rate [$s^{-1}cm^{-3}$]**
Cosmic rays	Planet boundary layer (PBL), i.e. up to 100-3000 m above ground	1-2
Alpha radiation emitted from the ground surface	a few cm above ground	unknown
Beta radiation emitted from the ground surface	a few meters above ground	0.1-10
Gamma radiation emitted from the ground surface	a few hundred meters above ground	1-6
Radiation from the radioactive gas radon and its daughters	1-2 m above ground	1-20

2.1.1 Radioactivity Originating from the Ground

Radioactivity originating from the ground can be further divided into two components. One component is the ionizing radiation that is emitted directly from the ground. Typically, the radiation consists of alpha and beta particles, and gamma rays. Alpha particles are the same as helium nuclei (i.e. consisting of two protons and two neutrons), beta particles are either electrons or positrons (which is the anti-particle of the electron, and has a charge of +1 e), and gamma rays are high energy electromagnetic waves. The emissions occur due to radioactive decay of radioactive materials such as uranium (U) and thorium (Th), that exist in the Earth's crust. However, the radiation emitted from these materials only cause ionization a few meter above ground. The other component is ionizing radiation that is emitted from the radioactive gas radon (Rn), and its daughters (i.e. decay products) [11]. The two radon isotopes Rn-222 and Rn-220 are parts of the uranium and thorium decay chains respectively, as displayed in Fig. 2.1 [14]. It follows that uranium and thorium cause ionization of air both directly due to ionizing radiation emitted from the ground surface, and indirectly by decaying into the air born radioactive gas radon.

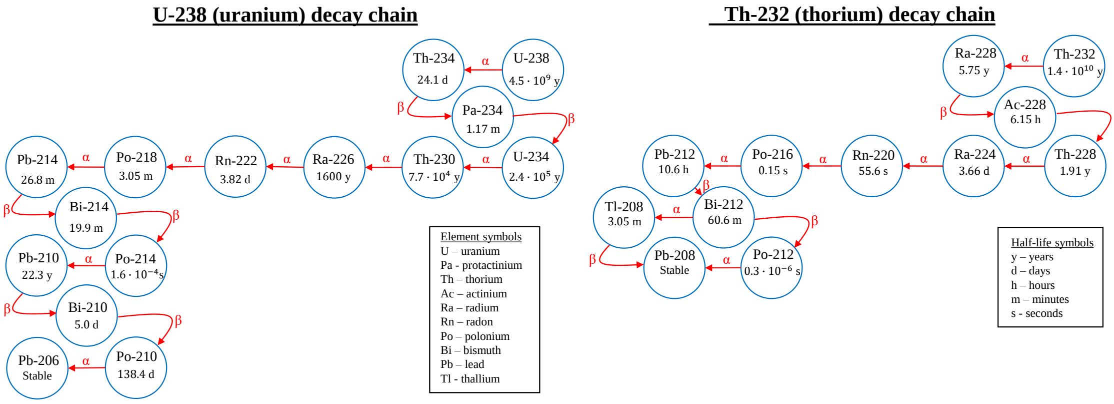

(a) **(b)**

Figure 2.1: Radioactive decay chains of **(a)** uranium, and **(b)** thorium, including isotope half-lives [15]. Only the main decay branches are indicated, and the symbols next to the branch arrows indicate alpha or beta mode of decay.

From Fig. 2.1 one can observe that both starting isotopes of uranium and thorium have half-lives of billions of years, and decay below the surface of the ground by through alpha and beta modes of decay. Often gamma-rays are emitted as well, depending on whether the daughter nucleus is left in an excited state or not [14]. As radon is reached in the decay chains, decay can transpire in air, since radon is an airborne gas. Both decay chains end in stable isotopes of lead (Pb). Another observation one can make from the figure, is that the Rn-222 isotope half-life of 3.82 days is significantly longer than the Rn-220 half-life of 55.6 s. Hence, Rn-222 exist in higher concentrations and is more important for ionization. Since radon is an airborne gas, it can emanate from the ground into the atmosphere, and more effectively ionize air molecules when it alpha decays. The concentration of radon in the air varies greatly with locations, since it depends on several factors such as the amount of uranium and thorium in the soil and rocks, the exhalation rate through the ground surface, and on the atmospheric dispersion [11]. Although both beta particle and gamma-ray (not shown in Fig. 2.1, but emissions of gamma-rays often follow alpha decay) radiation are also emitted in the decay chains of radon, the large majority of the energy is released as alpha particles [11]. Hence, an approximate expression for the rate of ionization due to the radioactive decay of Rn-222 is derived in the following text. First, a general equation for alpha decay can be expressed as

$$ {}^{A}_{Z}P \rightarrow {}^{A-4}_{Z-2}D +^{4}_{2} He + Q_\alpha \tag{2.1}$$

where P is the parent nucleus, A denotes the mass number (total number of protons and neutrons in the nucleus), Z denotes the atomic number (the number of protons in the nucleus), D is the daughter nucleus (decay product), ${}^{4}_{2}He$ is the emitted alpha particle (a helium nucleus) and Q_α is total kinetic energy released (alpha decay energy) [14]. Since an alpha particle consists of 2 protons and 2 neutrons, the atomic number of the daughter nucleus is 2 less than its parent, and the mass number is 4 less. The alpha decay energy Q_α is distributed according to

$$Q_\alpha = E_\alpha + E_{recoil} + E_\gamma \tag{2.2}$$

where E_α is kinetic energy [MeV] of the alpha particle, E_{recoil} is the kinetic energy [MeV] of the daughter nucleus due to the recoil effect as the alpha particle is emitted, and E_γ is the energy [MeV] emitted as gamma radiation if the daughter nucleus is left in an excited state [14]. Since energy and mass are conserved in the decay process, the alpha decay energy can be calculated by utilizing Einsteins mass-energy equivalence formula

$$E = mc^2 \tag{2.3}$$

where E is the energy [J], m is the mass [kg], and c = 299792458 m/s is the speed of light in vacuum [14]. In order to facilitate calculations, the speed of light squared (c^2) can be expressed in units of electronvolt divided by unified atomic mass unit [eV/u]

$$\begin{aligned} c^2 &= 299792458^2 \text{ J/kg} = \frac{299792458^2 \cdot 1.66053904 \cdot 10^{-27}}{1.60217657 \cdot 10^{-19}} \text{ eV/u} = \\ &= 931.494 \text{ MeV/u} \end{aligned} \tag{2.4}$$

where 1 eV = $1.60217657 \cdot 10^{-19}$ J, and 1 u = $1.66053904 \cdot 10^{-27}$ kg. By inserting (2.4), and numeric values for atomic mass (from [16]) of Rn-222, its daughter Po-218 (see Fig. 2.1) and an alpha particle into (2.3), the decay energy of Rn-222 can be calculated as

$$\begin{aligned} Q_\alpha =& (M_{222_{Rn}} - M_{218_{Po}} - M_\alpha)c^2 = \\ =& (222.0175782 - 218.0089735 - 4.002603254) \text{ u} \cdot 931.494 \text{ MeV/u} = \\ =& 5.5903 \text{ MeV} \end{aligned} \tag{2.5}$$

where $M_{222_{Rn}}$, $M_{218_{Po}}$, and M_α are the atomic masses of Rn-22, Po-218 and an alpha particle respectively. The recoil energy of the daughter nucleus in (2.2) can be calculated utilizing the following non-relativistic expression (see [14] for a derivation)

$$E_{recoil} = \frac{M_\alpha}{M_{recoil}} \cdot E_\alpha \tag{2.6}$$

where M_{recoil} is the mass [u] of the daughter nucleus [14]. If (2.6) is substituted into (2.2), and if the gamma-ray energy is set to zero (since 99.92 % of the Rn-222 decays result in 0 eV excitation level of the daughter, and hence no gamma-ray is emitted [16]), the energy of the emitted alpha particle can be found as

$$E_\alpha = \frac{M_{recoil}}{M_{recoil} + M_\alpha} \cdot Q_\alpha = 5.4895 \text{ MeV} \tag{2.7}$$

As the positively charged alpha particle traverse through the air, it can ionize air molecules, i.e. removing electrons, by either Coulomb attraction (since the alpha particle is positively charged) or by direct collision [14]. An estimate of the number of ion pairs produced due to one alpha particle can be calculated as

$$\frac{5.4895 \text{ MeV}}{35 \text{ eV/ion pair}} = 1.5684 \cdot 10^5 \text{ ion pair} \tag{2.8}$$

where 35 eV/ion pair is the average energy required of an alpha particle to produce one air ion pair [14]. Finally, the ionization rate due to the alpha decay of Rn-222 alone (not including Rn-220 or any of their progeny) can be approximated as

$$q_{Rn-222} = 1.5684 \cdot 10^5 \text{ ion pair} \cdot (\text{radon radioactivity concentration}) \tag{2.9}$$

where q_{Rn-222} is the ionization rate [$\text{s}^{-1}\text{cm}^{-3}$] due to Rn-222 radioactivity (radon radioactivity concentration) [Bq/cm^3].

The ionizing radiation from the radon daughters are also important for the ionization of air. Due to the recoil effect that accompanies alpha decay, electrons are removed from the parent atom, hence the radon daughters are positive ions [14]. Quickly after the radioactive decay, the positively charged daughter radionuclide form clusters with water vapor and trace gases. In turn, these radioactive cluster ions can attach to aerosols (solid or liquid particles suspended in the air) and remain in the air until they decay, or they can be transferred to surfaces by either wet or dry deposition and decay there instead. Wet deposition include collision between aerosol particles and water vapor, which causes the aerosol particles to be transferred to the ground surface. Dry deposition includes impaction, diffusion, and sedimentation [14]. Where impaction is the inability of an aerosol particle to follow a sharp turn in an air stream due to its own inertia and instead hit a surface, diffusion is the movement from regions of high concentration to regions of low concentration, and sedimentation is collection on surfaces due to gravity. Finally, whether the radon daughters decay suspended in the air or on a surface can affect the ionization of air.

2.1.2 The Ion Balance Equation

The ionization, primarily due to radiation, cause a neutral air molecule, e.g. oxygen or nitrogen, to be split into a positive ion and an electron. In turn, a negative ion is quickly formed due to attachment of the electron to neutral air molecule [11]. Next, in the order milliseconds, these positive and negative ions undergo several different reactions with other molecules in the air. Including chemical, charge exchange, and clustering reactions, which causes the ions to finally form clusters denoted small ions [11]. Typically, these clusters contain several water vapor molecules, depending on the level of humidity. In Table 2.2 some examples of positive and negative small cluster ions located at low altitudes are presented [13].

Table 2.2: Examples of positive and negative small cluster ions located at low altitudes. n denotes the number of attached water vapor molecules which depends on the humidity, and varies typically between 4 and 8 [13].

Positive small cluster ions	**Negative small cluster ions**
$H_3O^+(H_2O)_n$	$O_2^-(H_2O)_n$
$H^+(H_2O)_n$	$CO_4^-(H_2O)_n$

The concentration of small ions is determined by the balance between ion generation and deionization processes. Ion generation is primarily due to the different radiation sources described in the previous subsections. Deinization is caused primarily by two different processes. One is ion-ion recombination, a process in which neutral molecules are formed by reactions of ions. The other process involves aerosols, which are particles suspended in air or other gases [11]. Examples of aerosol include dust and fog. Small ions can be annihilated by aerosol in two ways, either by attachment to an aerosol particle or by recombining with another ion already attached to an aerosol [11]. Assuming equal densities of both positive and negative ions, and no electric fields, the dynamics of the small ion concentration in air can be expressed using the simplified ion balance equation

$$\frac{\partial n}{\partial t} = q - \alpha n^2 - \beta n Z \tag{2.10}$$

where $n = n_+ = n_-$ [cm^{-3}] is the concentration of both positive and negative ions, q is a source term that represents the rate of ion generation [$s^{-1}cm^{-3}$] due to radiation, electron attachment, and ion detachment from aerosols [11]. Deionization processes are constituted by two sink terms. One term contains the recombination coefficient α [cm^3s^{-1}] that represents ion-ion recombination, a process in which neutral molecules are formed by reactions of ions [11]. The other term contains the effective ion-aerosol attachment coefficient β [cm^3s^{-1}], which describes the probability than a small ion attaches to an aerosol or recombines with an ion attached to the aerosol [11]. Z is the total aerosol concentration [cm^{-3}]. Aerosols particles (e.g. fog particles) are large and immobile, and the concentration varies strongly with location. Charged aerosols are formed by attachment different types of charge carriers, such as ions or electrons on aerosol particles.

Equilibrium conditions in small ion concentration occur when the rate of ion generation is equal to the rate of deionization. From the ion balance equation (2.10) one can deduce that under equilibrium conditions, i.e. $\partial_t n = 0$, and in areas with negligible pollution ($Z = 0$), the small ion density can be found as

$$n_{eq} = \sqrt{\frac{q}{\alpha}} \tag{2.11}$$

where n_{eq} is the equilibrium concentration [cm^{-3}] of both positive and negative ions. However, it should be noted that the ratio between positive and negative small ions typically are not unity. Instead, the ratio is around 1.12 near the ground due to the atmospheric electrode effect [17]. In Table 2.3 some typical literature values are presented for the different coefficients in the ion balance equation (2.10) [18]. As can be observed in the table, typical values for the total aerosol concentration varies greatly. For high aerosol concentrations the deionization process will be dominated by last term in (2.10), i.e. ion-aerosol attachment.

Table 2.3: Typical values for the variables and coefficients in the ion balance equation (2.10) [18].

Symbol	Description	Typical value
n	Ion concentration	2500 [cm^{-3}] (very clean conditions)
q	Rate of ion generation	10 [$\mathrm{s}^{-1}\mathrm{cm}^{-3}$]
α	Recombination coefficient	$1.5\cdot10^{-6}$ [$\mathrm{cm}^3\mathrm{s}^{-1}$]
β	Attachment coefficient	$1\text{-}2\cdot10^{-6}$ [$\mathrm{cm}^3\mathrm{s}^{-1}$]
Z	Total aerosol concentration	200 [cm^{-3}] (very clean conditions) 10^5 [cm^{-3}] (polluted urban air)

2.2 Electrical Conductivity of Air

The conductivity of a medium is a measure of its ability to transport charges under the influence of an electric field, i.e. to conduct an electric current [19]. This can be expressed by means of the generalized form of Ohm's law

$$\vec{J} = \sigma \vec{E} \tag{2.12}$$

where $\vec{J}$ is the current density vector [A/m^2], $\vec{E}$ is the electric field vector [V/m], and σ is the electrical conductivity [S/m] [19]. As is evident from (2.12), the flow of conduction current in air is determined both by the strength and direction of the electric field and by the conductivity. In turn, the conductivity is determined by the concentrations of charge carriers, and their respectively mobilities and electric charge. By taking into account the concentrations of all charge carriers of different mobilities, the total conductivity of air can be expressed as

$$\sigma = \sigma_+ + \sigma_- = e\left(\sum_i \mu_i^+ n_i^+ + \sum_i \mu_i^- n_i^-\right) \tag{2.13}$$

where e is the elementary charge $1.602 \cdot 10^{-19}$ C, μ is the mobility [m^2/Vs], n is the charge carrier concentration [cm^{-3}], subscript i denotes charge carrier type, and superscript + or - denotes charge polarity [10]. Charge carrier types can be divided into electrons, positive and negative ions of different sizes, and charged aerosols. A typical division of charge carriers in air with respect to radius and mobility, is presented in Table 2.4 [9]. For air, small ions are consider to contribute to the large majority of the air conductivity, due to their fast mobilities [12]. In contrast, free electrons only exist for a very short time in air, hence do not contribute to the conductivity and can be neglected [10]. Furthermore, the mobility is a measure of the ability of a charge carrier to move through a medium under the influence of an electric field, and is defined as

$$\mu = \frac{|\vec{v}_d|}{|\vec{E}|} \tag{2.14}$$

where $\vec{v}_d$ is the drift velocity vector [m/s], i.e. the speed and direction with which charge carriers travel under influence of an electric field [12]. The mobility is generally proportional to the size of the charge carrier, i.e. smaller carriers such as electrons or small ions have higher mobility values in comparison with larger carriers such as charged aerosols (see Table 2.4).

The conductivity of air is not constant. Instead, the conductivity is field dependent, as is illustrated in the current-voltage characteristic for air, presented in Fig. 2.2 [5]. The characteristic can be divided into three regions: Ohmic, sweep-out, and Townsend discharge region. The Ohmic region is for voltages between 0 and V_1, where it can be observed that the curve is approximately linear. This means that the conductivity of air is approximately constant under the influence of weak electric fields. Next, the sweep-out region is for voltages between V_1 and V_2, where the curve is approximately horizontal, i.e. the conductivity is decreasing as the voltage is increased. This is due to the sweeping out effect of air ions, i.e. the electric field accelerates the ions towards respective electrode faster than new ions are generated. The maximum current in this region i_0, is determined by the rate of ion generation. The final region is the Townsend discharge region, which is for voltages above V_2. In this region the current increases exponentially, due ion injection by means of Townsend discharges, e.g. corona discharges in a non-uniform field. This means that the electric field is strong enough to cause Townsend discharges, which generates air ions, which in turn increases the conductivity according to (2.13), and current density according to (2.12).

Table 2.4: Division of charge carriers in air with respect to radius and mobility range [9].

Charge carrier	**Radius range [m]**	**Mobility range [m^2/Vs]**
Small ion	$< 10^{-9}$	10^{-5} to $2 \cdot 10^{-4}$
Medium ion	10^{-9} to $2 \cdot 10^{-8}$	10^{-7} to 10^{-5}
Charged aerosol (large ion)	$2 \cdot 10^{-8}$ to $2 \cdot 10^{-7}$	10^{-9} to 10^{-7}

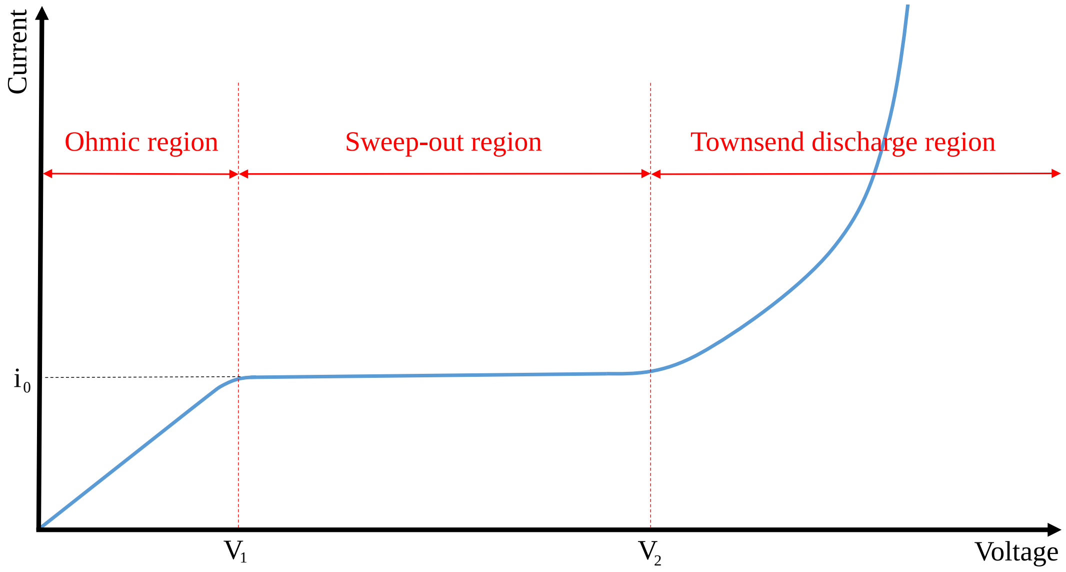

Figure 2.2: General current-voltage characteristics for air [5].

In order to express the dynamics of the charge carrier concentrations in the presence of electric fields, the ion balance equation (2.10) can be modified by expressing the concentration for each polarity of small ions and charged aerosol separately, and by adding current density terms to form the following simplified ion-aerosol balance equations

$$\frac{\partial n_+}{\partial t} + \nabla \cdot \vec{j}_+ = q - \alpha n_- n_+ - n_+ \beta (Z - N_+) \tag{2.15}$$

$$\frac{\partial n_-}{\partial t} + \nabla \cdot \vec{j}_- = q - \alpha n_+ n_- - n_- \beta (Z - N_-) \tag{2.16}$$

where $n_\pm$ are the concentrations of positive and negative small ions [cm^{-3}], Z is the total aerosol concentration [cm^{-3}] and is defined as

$$Z = N_0 + N_+ + N_- \tag{2.17}$$

where N_0, N_+ and N_- are the concentrations [cm^{-3}] of neutral, positively and negatively charged aerosols respectively [10]. The divergence of the current density vectors, $\nabla \cdot \vec{j}_\pm$ represent the movement of charge carriers due to both applied electric fields and diffusion. The current densities vectors are expressed as

$$\vec{j}_\pm = \pm \mu_\pm n_\pm \vec{E} - D_\pm \nabla n_\pm \tag{2.18}$$

where the left term on the right hand side represent the drift currents, i.e. charge carriers accelerated by electric fields [10]. The right term on the right hand side represent the diffusion currents, which are inversely proportional to the gradient of the ion concentration. Diffusion is the tendency of ions in regions of high concentration to spread (diffuse) into regions of the air containing less concentration. $D_\pm$ are the diffusion coefficients [m^2s^{-1}] and can for low electric fields be expressed by the Einstein relation

$$D_\pm = \frac{\mu_\pm k_B T}{q} \tag{2.19}$$

where k_B is Boltzmann's constant $1.38 \cdot 10^{-23}$ JK^{-1} and T is the absolute temperature [K] [10]. If the level of pollution is low, the effect of aerosols can be neglected, hence (2.15) and (2.16) reduces to the following set of ion balance equations

$$\frac{\partial n_+}{\partial t} + \nabla \cdot \vec{j}_+ = q - \alpha n_- n_+ \tag{2.20}$$

$$\frac{\partial n_-}{\partial t} + \nabla \cdot \vec{j}_- = q - \alpha n_+ n_- \tag{2.21}$$

Finally, the electric potential and field distribution can be coupled to the ion concentrations by means of Poisson's equation (2.22) and the definition of electric potential (2.23)

$$\nabla \cdot (-\epsilon \nabla \phi) = e(n_+ - n_-) \tag{2.22}$$

$$\vec{E} = -\nabla\phi \tag{2.23}$$

where ϕ is the electric potential [V] and ϵ is the permittivity [19].

3

The Ion Box

This chapter presents the ion box used for the experiments conducted for this thesis. Special attention is given to the instruments measuring electrical related quantities, which are given their own sub-chapters.

3.1 Layout Overview and Installed Measuring Instruments

The ion box is a data acquisition (DAQ) system based around the measurement of both positive and negative air ion concentrations. In addition, several other measuring instruments are installed in the ion box, in order to measure physical quantities that could be related to the ion concentrations. In Fig. 3.1 two photographs of the ion box with the protective lids open are displayed. In the figure the different measuring instruments installed are highlighted. The measured physical quantities can roughly be divided into three categories: electrical, environmental and monitoring related quantities. Electrical related quantities include air ion concentrations, DC and AC electric field strengths, and ion current. Environmental related quantities include temperature, humidity, air pressure, illumination, air flow, air pollution, radon radioactivity, gamma radiation, motion detectors, and acceleration sensors. Monitoring related quantities include temperature sensors inside the ion box, DC voltage supply, cooling fan speed, differential pressure for the air ion counters, and voltage pulses to the air ion counters. Some of the sensors are not visible in Fig. 3.1, since they are located inside the ion box.

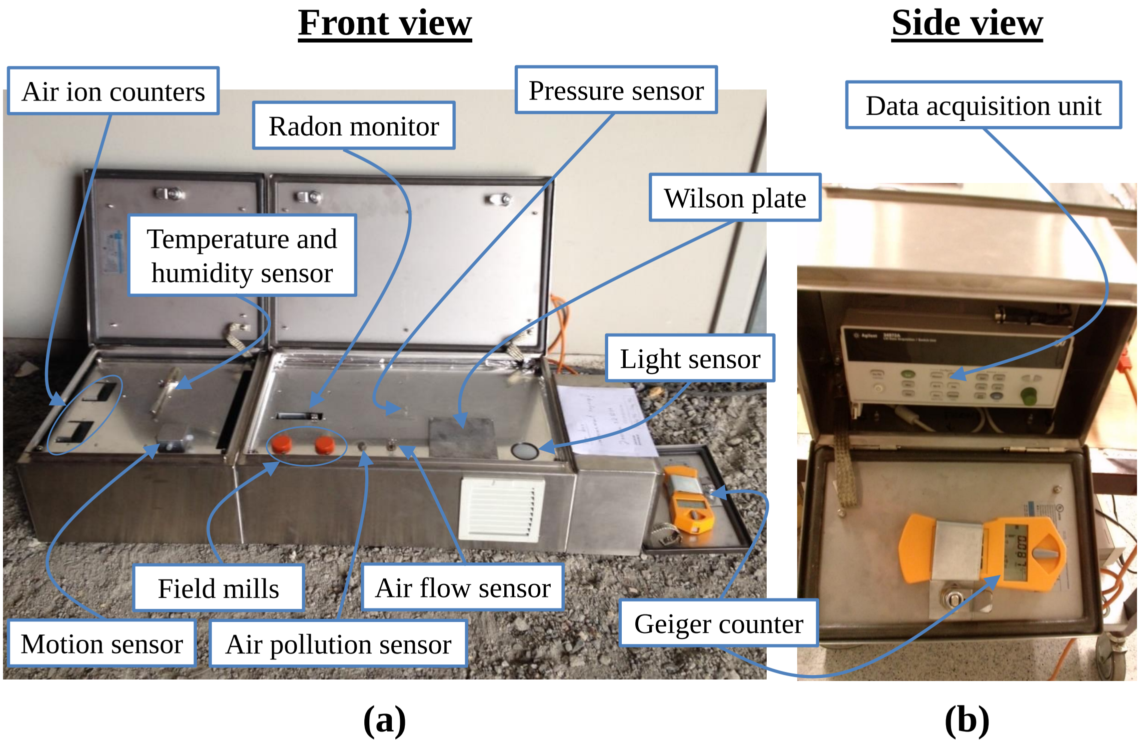

Figure 3.1: Photographs of the ion box with the lids open **(a)** from the front, and **(b)** from the side. Indicated are the different instruments installed in the ion box.

In Fig. 3.1 (b), the DAQ unit, an Agilent 34972A from the United States based company Agilent Technologies is displayed. It samples and stores data from all measuring instruments excluding the Geiger counter and the radon monitor, since they are not compatible with the DAQ unit. The sampling period of the DAQ is 2 seconds, and the data is stored from 35 channels on a USB flash drive. The data on the USB flash drive can be read by a computer, and displayed using a post-processing software of choice. The data from the Geiger counter and radon monitor must be downloaded separately to a computer using USB cables, together with the respectively manufacturers software. Finally, in order to operate the ion box, it needs to be connected to a 230 V power supply.

In Table 3.1 a list of the measuring instruments utilized for measuring electrical and environmental quantities, installed in the ion box is presented. The measuring instruments for electrical related quantities (the three first rows in the table) are described separately in subsequent chapters, whereas the instruments measuring environmental quantities are described briefly in the following text. The instruments are explained in the order they are listed in the table. On the 4th row from the top in Table 3.1, the MP Motion Sensor is listed. Four sensors are installed in four different directions (see Fig. 3.1), in order to be able to detect movement by e.g. people or animals in the close vicinity of the ion box, which in turn might affect the ion concentration. They can be used as tools for e.g. correlating perturbations in the ion concentrations during long term measurements (that otherwise would be difficult to interpret), with movement of people in the vicinity of the ion box. The sensors are of a pyroelectric material that generates a voltage as it is exposed to changes in infrared radiation, due to e.g. people [20]. The motion sensors installed in the ion box are configured to output 5 V if motion is registered, otherwise 0 V. On the 5th row from the top in the table, the HS-135 Air Pollution Sensor is listed. It is used to measure different types of air pollution such as smoke, sulfur dioxide (SO_2), carbon dioxide (CO_2), isobutane (C_4H_{10}) and alcohol. The concentration of air pollution is relevant to measure since it contributes to deionization, as explained in sub-chapter 2.1.2. The HS-135 is a tin dioxide (SnO_2) semiconductor sensor, which change its resistance value depending on the gas composition. The output signal is a voltage that is converted to a value of gas concentration in ppm (parts per million), utilizing a characteristics curve. Each detectable gas has a different characteristics curve [21].

On the 6th row from the top in Table 3.1, the light sensor is listed. The sensor is extracted from a Mastech Digital Luxmeter MS 6610 (only the sensor is installed in the ion box, not the rest of the instrument). It measures illuminance in lux [lx] (which is the same as lumen per square meter [lm/m^2]), and can be utilized to e.g. observe when light sources are switched on/off in indoor measurements, or when the ion box is subjected to direct sunlight in outdoor measurements. On the 7th row from the top in the table, the PTU303 Combined Pressure, Humidity and Temperature Transmitter is listed. These are all parameters representing the atmospheric conditions, and should be recorded when performing e.g. electric field measurements [9]. Additionally, the humidity is known to affect the ion concentrations [29]. On the 8th row from the top in the table, the Acceleration Sensor KAS901 is listed. It is utilized in order to see if the ion box is moved or shoved, which naturally can affect any measurement. Both a single- and a dual-axis sensor is installed in the ion box, in order to cover acceleration along all three axis in a Cartesian coordinate system. On the 9th row from the top in the table, the air flow sensor is listed. It is constructed by ABB Corporate Research, and functions by measuring the temperature difference between two NTC thermistors. Through one of the thermistors an electric current flows in order to heat it up, while the other thermistor is not heated by a current. As wind blows the heated up thermistor will be cooled down, while the non-heated thermistor is unaffected. Hence the temperature difference between the thermistors is proportional to the air flow.

Table 3.1: A list of the different measuring instruments, utilized for measuring electrical and environmental quantities, which are installed in the ion box.

Instrument	**Manufacturer**	**Measured quantity**	**Sampled by the DAQ unit?**
Air Ion Counter	AlphaLab, Inc.	Air ion concentration [ions/m^3]	Yes
Field Mill EFM 113B	Kleinwächter GmbH.	DC electric field strength [V/m]	Yes
Wilson plate	-	Ion current [A] and AC electric field strength [V/m]	Yes
MP Motion Sensor AMN (NaPiOn) series, standard type	Panasonic Electric Works	Indicates movement by outputing a 5 [V] signal	Yes
HS-135 Air Pollution Sensor	Sencera Co. Ltd.	Gas concentration [ppm]	Yes
Light sensor (Digital Luxmeter MS 6610)	Precision Mastech	Illuminance [lx]	Yes
PTU303 Combined Pressure, Humidity and Temperature Transmitter	Vaisala	Air pressure [kPa], relative humidity [%] and temperature [°C]	Yes
Acceleration Sensor KAS901	KELAG Künzli Elektronik AG	Acceleration [g]	Yes
Air flow sensor (utilizing two NTC thermistors)	-	Outputs a voltage signal [V] proportional to the air flow	Yes
Geiger counter	Gamma-Scout GmbH & Co. KG	Gamma radiation, dose rate [µSv/h]	No
R1 Radon Monitor	Radonelektronik AB	Radon radioactivity concentration [Bq/m^3]	No

Two of the measuring instruments are not connected to the DAQ unit, i.e. the R1 Radon Monitor and the Gamma-Scout Geiger counter. These instruments are listed on the two last rows of Table 3.1. The Geiger counter, set to measure gamma radiation, is mounted on the side lid of the ion box, beside the DAQ unit. It is based on the Geiger-Müller counter tube, and measures the number of counts (the number of ionized atoms or molecules) per unit time (i.e. pulse rate), due to ionizing radiation [22]. The pulse rate is then converted into the dose equivalent unit µSv/h (microsievert per hour), by use of the Cs-137 isotope as reference. The R1 Radon Monitor from the Swedish company Radonelektronik AB, which measures the radioactivity due to radon, is also installed in the ion box. The working principle can be described as follows. First, air diffuses through a filter which removes the radon daughters, then as Rn-222 decays the ionized daughter product Po-218 is attracted to a semiconductor detector by an electric field. As Po-218 decays the emitted alpha particle is detected by the semiconductor detector. Hence the activity concentration of Rn-222 can be determined, since Rn-222 always decays into Po-218 [23].

The different measured monitoring functions of the ion box are presented in Table 3.2. The functions in the first two rows are related to the method of offset calibration for the air ion counters. The calibration works by automatically turning off the 5 V supply voltage for 1 min to the air ion counter fans, and by setting the polarity switch to zero. The idea is that one should average the ion concentration in a post-processing software during this 1 min calibration period, in order to determine the offset. If the average value is zero, then there is no offset. The automated turn on/off of the air ion counters repeats every 35 min. The voltage to the air ion counters are measured so that one can see when they are turned on/off. By observing the differential pressure at the same time, one can determine if the air flow changes (which it should). Additional measurements that can be utilized in order to determine the status of the ion box are listed in the last three rows of the table. The temperatures inside the two main compartments of the ion box are measured with thermocouples, in order to e.g. see if the ion box gets overheated. The DC supply voltages are measured to be able to monitor that each one has the right value, and in turn that the various instruments is supplied with the right voltage. Finally, the voltage over the ion box cooling fan is measured, so that one can determine whether it functions properly or not.

Table 3.2: A list of the measured monitoring functions for the ion box.

Measured monitoring function	**Measured quantity**	**Sampled by the DAQ unit?**
Air ion counters turn on/off for offset calibration	Voltage [V]	Yes
Differential pressure sensors (Smartec B.V. type SPD102DAhyb) are used to detect changes in air flow through the air ion counters	Differential pressure [bar]	Yes
Temperatures inside the compartments of the ion box	Temperature [°C]	Yes
DC supply voltages +5V, +15V, and -15V	Voltage [V]	Yes
Speed of ion box cooling fan	Voltage [V]	Yes

3.2 Aspiration-type Air Ion Counter

Two aspiration-type air ion counters from the United States based company AlphaLab, Inc are installed in the ion box, where aspiration-type refers to the use of forced air flow though the measuring device. The reason for having two air ion counters installed is to be able to independently measure both the positive and negative ion density. A photograph of an air ion counter is displayed in Fig. 3.2 (a), where it can be observed that the front panel has a digital display and options for e.g. measuring range and polarity (In Fig. 3.1 the top part of the two air ion counters installed in the ion box are visible). Although they can be used as portable devices, i.e. displaying the measured ion concentration on the digital displays, in the ion box the analog output signal is instead utilized. Furthermore, in Table 3.3 some selected data for the installed air ion counters are presented. In addition to the standard 2 million ions/cc (ions per cubic centimeter) version mounted in the ion box, 20 and 200 million models also exist [24]. In the table one may also notice the rather large measurement uncertainty (accuracy), which is primarily due to the turbulent air flow at the wind guard that causes ions to neutralize each other [24]. The wind guard is a small removable metallic piece that is mounted on top of the instrument, visible in Fig. 3.1 (the metallic part contrasting the otherwise black air ion counters). The reason for keeping the wind guard is to avoid measurement errors due to too high wind speeds and external electric fields [24]. The different noise levels presented for the different ranges determine the effective resolution of the measurements, when using the analog output signal [25]. Finally, the specified critical mobility is another important parameter since it determines which size of ions are being measured.

Table 3.3: A selection of data for AlphaLab's air ion counter [24].

Manufacturer	AlphaLab Inc.
Product model	Air Ion Counter, standard 2 million ions/cm^3 version
Technology	Based on the Gerdien condenser (tube)
Range/resolution [ions/cm^3] (the specified resolution is for the digital display)	Three different options are available: 20,000/10 200,000/100 2,000,000/1000
Accuracy	±25 % of reading
Approximate noise levels [ions/cm^3] at the different range selections [25]	10 for the 20,000 range 30 for the 200,00 range 100 for the 2,000,000 range
Critical mobility μ_c [m^2/Vs] [26]	$8 \cdot 10^{-5}$

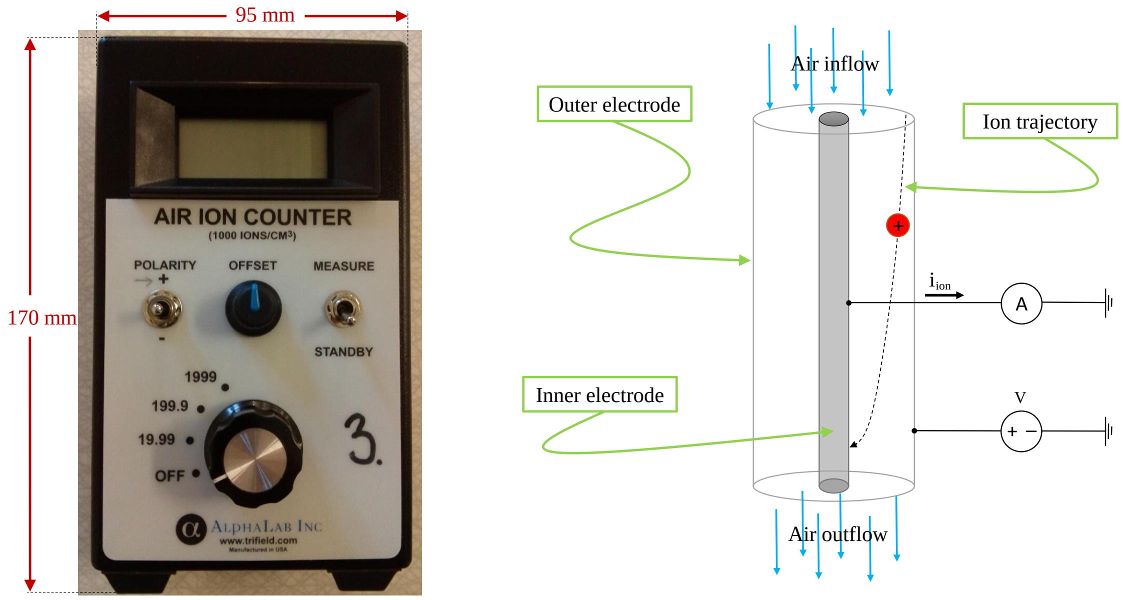

(a) **(b)**

Figure 3.2: **(a)** A photograph of the standard 2 million ions/cm^3 version AlphaLab air ion counter, and **(b)** a schematic figure of a cylindrical Gerdien condenser for the case when it is set to measure positive ions (which is characterized by the applied voltage V being positive).

As specified in Table 3.3, the technology utilized in the air ion counter in order to measure the ion concentration is based on the Gerdien condenser. In contrast to the original design, in which the rate of decay of a voltage between two electrodes is measured, the modern interpretation of the Gerdien condenser instead measures the ion current [27]. The working principle can be explained by referring to Fig. 3.2 b). A fan is used to create an air flow (illustrated by yellow arrows in the figure) through the Gerdien condenser at a known rate. Naturally, air ions will follow the flow of air through the condenser. The figure also displays two electrodes. One outer cylindrical electrode to which a potential is applied. The polarity of the applied potential depends on which polarity of ions should be measured. The figure exemplifies the case when positive ions are measure, hence a positive potential is applied to the outer electrode (if negative ions are to be measured a negative potential is applied instead). The other electrode is the inner electrode, which is at ground potential. As air is sucked into the condenser, positive ions will be attracted to the inner electrode by the force of the electric field created by the potential difference between the electrodes. Whether an ion reach the inner electrode (and hence is measured) or not depends on both its spatial position when entering the cylinder, and on its mobility in relation to the critical mobility μ_c of the Gerdien condenser

$$\mu_c = \frac{M_0 \epsilon_0}{VC} \tag{3.1}$$

where M_0 is the known volumetric air flow rate [cm^{3}s^{-1}] through the cylinder, V and C are the voltage [V] and the capacitance [F] between the electrodes respectively [9].

All charge carriers with mobilities equal to, or exceeding the critical mobility, will be collected by the inner electrode, whereas only a fraction of the charge carriers with mobilities lower than the critical mobility will be collected. This can be explained by referring to the definition of electric mobility (2.14), i.e. the drift velocity towards the inner electrode increase with increasing mobility. Hence lower mobility ions will not have enough time to reach the inner electrode, before they have reached the end of the cylinder by the influence of the air flow. From (3.1) it can be deduced that the critical mobility can be decreased by either decreasing the air flow rate, or by increasing the polarizing voltage between the electrodes, and consequently a larger fraction of lower mobility air ions will be collected, and vice versa. The ions that reach the inner electrode will flow to ground through the electrometer, which measures the ion current

$$i_{ion} = M_0 e \left(\int_0^{\mu_c} \frac{\mu}{\mu_c} f(\mu) d\mu + \int_{\mu_c}^{\infty} f(\mu) d\mu \right) \tag{3.2}$$

where i_{ion} is the measured ion current [A], e is the elementary charge [C], and f(μ) is the mobility distribution function [9]. The left integral represents the concentration of ions with mobilities below the critical mobility, that is collected at the inner electrode. Only a fraction of these ions are collected, depending on their spatial position when entering the cylinder. The right integral represent the concentration of ions with mobilities exceeding the critical mobility, out of which all are collected at the inner electrode. By design of the Gerdien condenser a critical mobility is achieved so that the desired size of ions are measured. Hence, the integrals in (3.2) can be represented by the ion concentration n [cm^{-3}] of ions with mobilities equal to, or exceeding the critical mobility, together with a fraction of lower mobility ions. Finally, assuming all ions are singly charged, the ion concentration of one polarity can be calculated as

$$n = \frac{i_{ion}}{e M_0} \tag{3.3}$$

Finally, the offset adjust procedure for the air ion counters is described in the last paragraph of the previous section.

3.3 Shutter-type Field Mill

The ion box is equipped with two sensors for measuring DC electric field strength. The sensors are shutter-type field mills from the German company Kleinwächter GmbH, and one of them is displayed in Fig. 3.3 (a). In Fig. 3.1 the placement of the two field mills installed in the ion box can be deduced (in the figure the orange shield caps are on). Additional data on the field mills are presented in Table 3.4. From the table one can deduce that the two field mills installed in the ion box have different measuring ranges, and different sensitivity in order to complement each other. The field mills only measure the field strength at ground potential, and in order to get an accurate reading, the sensors should be placed perpendicular to the incident electric field lines. A positive electric field is defined as field lines pointed down into grounded instrument, from a positive HV source. Furthermore, the field mills provide no other information regarding electric field distribution.

Table 3.4: A selection of data for Kleinwächter GmbH's field mill [28].

Manufacturer	Kleinwächter GmbH
Product model	EFM 113B
Technology	Shutter-type field mill
Available measuring ranges [kV/m]	5, 20, 50 and 200
Measuring ranges [kV/m] selected for the two field mills installed in the ion box	Field mill 1: 200 Field mill 2: 5
Measuring precision	5 % in a homogeneous field

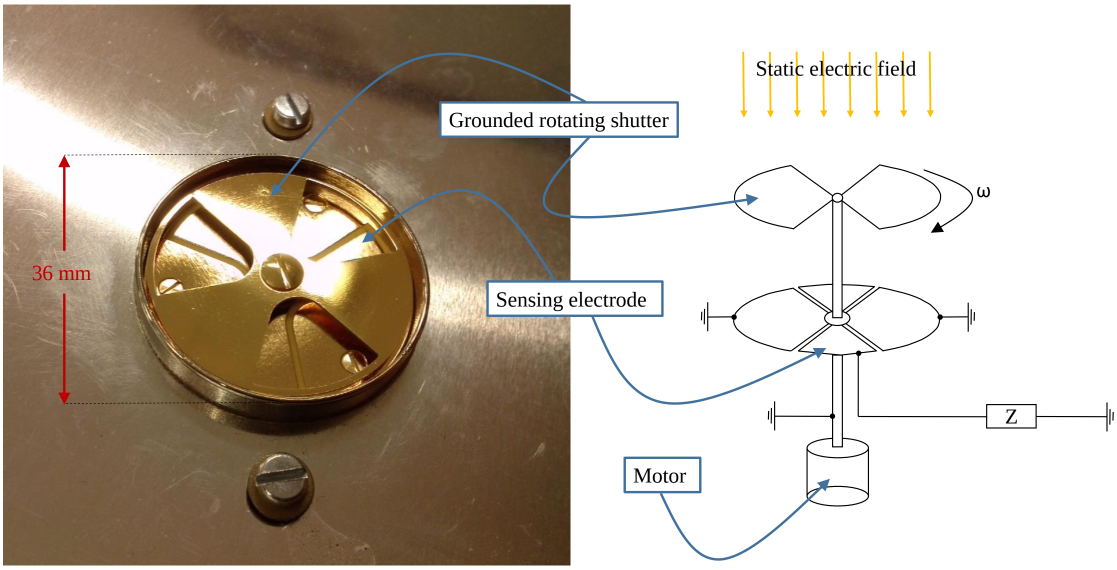

(a) **(b)**

Figure 3.3: **(a)** A photograph of one of the field mills installed in the ion box, and **(b)** a schematic figure of a shutter-type field mill illustrating the working principle.

The working principle of a field mill can be explained by referring to Fig. 3.3 (b). By exposing the sensing electrode in the figure to an electric field, surface charges will be induced that cancels the field inside the conductive body [19]. This phenomena is expressed by the boundary conditions for a conductive body and air interface, assuming an irrotational electric field

$$E_t = 0 \tag{3.4}$$

$$E_n = \frac{\rho_s}{\epsilon_0} \tag{3.5}$$

where E_t and E_n denotes tangential and normal components respectively of the electric field [V/m] external to the conductive body, and ρ_s is the surface charge density [C/m^2] [19]. The movement of charges during the accumulation of surface charges is a current that can be measured, but it will only flow a current when there is a change in the normal component of the incident electric field, and hence in the surface charge distribution. It follows that for a static field, the surface charge distribution is at an equilibrium, and there is no current to be measured. In the shutter-type field mill, this problem is solved by utilizing a grounded rotating shutter that periodically exposes and shields the sensing electrode from the electric field [9]. Consequently, a time dependent charge which are proportional to the electric field is induced, and can be expressed as

$$q_s(t) = \epsilon_0 E_n a(t) \tag{3.6}$$

where q_s(t) is the induced time dependent charge [C], and a(t) is the time dependent area [m^2] of the sensing electrode that is exposed to the electric field [9]. How the area change with time depends on the rotating speed of the rotating shutter, together with the shape and dimensions of the sensing electrode and rotating shutter. By utilizing the definition of electric current, and solving for the normal component of the electric field strength, (3.6) can be rewritten as

$$i_s(t) = \frac{dq_s(t)}{dt} = \frac{d(\epsilon_0 E_n a(t))}{dt} \Rightarrow E_n = \frac{i_s(t)}{\epsilon_0 \frac{d(a(t))}{dt}} \tag{3.7}$$

where $i_s(t)$ is the induced current [A] that flows due to changes in the induced surface charge distribution. Finally the electric field strength can be determined by e.g. measuring the voltage drop over the impedance Z in Fig. 3.3 (b) in order to obtain the induced current [9].

Normally the field mills should be offset adjusted by the use of a potentiometer included in the design. This is done by first shielding the field mills with grounded caps that ensures zero electric field strength, and then adjusting the potentiometer through a hole on the backside of the device, so that zero output current is measured. But since the field mills are installed in the ion box, the potentiometer is not easily reached, and offset adjust instead has to be done in a post processing software. By initiating each measurement with the grounded caps on the field mills, one achieves a reference for zero electric field strength. The offset adjust is then easily accomplished by subtracting the value measured with the grounded caps on.

3.4 Wilson Plate

The ion box has a Wilson plate of dimensions 127 mm^2 installed on top of the ground plane (as opposed to flush with the ground plane), which is utilized for measurement of both ionic current and AC electric field strength. The plate was designed by ABB Corporate Research for the ion box, and is displayed in close up in Fig. 3.4 (a). Its placement in the ion box can be observed in Fig. 3.1 (a). This Wilson plate is not designed for sensitive measurements, hence the voltage signals are measured by the DAQ, and not a more sensitive electrometer.

Basically, the Wilson plate consists of a current sensing surface connected to ground via a resistor and a capacitor in parallel, as illustrated in Fig. 3.4 (b). For the ion current measurement, the DC voltage over the resistor and capacitor displayed in the figure is measured. For the AC electric field strength measurement, the AC rms voltage is measured instead. The working principle of the ion current measurement is very simple, and can be explained as follows. As the Wilson plate is placed in a electric field, air ions will travel along the field lines to the current sensing surface, as displayed in Fig. 3.4 (b). As the ions reach the sensing surface, the electric charges will flow to ground. In turn, the current causes a voltage drop over the resistor. Hence the voltage drop can be measured, and is proportional to the ion current. The measured total current has two contributions, i.e. ion current (3.8) and displacement current (3.9)

$$i_{ion} = \vec{J}_{ion} \cdot \vec{A} = \sigma \vec{E} \cdot \vec{A} = e(\mu_+ n_+ + \mu_- n_-)\vec{E} \cdot \vec{A} \tag{3.8}$$

$$i_{disp} = \vec{J}_{disp} \cdot \vec{A} = \epsilon_0 \frac{\partial \vec{E}}{\partial t} \cdot \vec{A} \tag{3.9}$$

where i_{ion} and i_{disp} are the ion and displacement currents [A] respectively, $\vec{J}$ denotes the current density vector [A/mm²], and $\vec{A}$ is the surface area vector [m^2] of the Wilson plate. Finally, offset calibration of the ion current measurement can be performed in the following way. First, measure the ion current with the lids of the ion box closed. Then calculate the average of the ion current signal in a post-processing software, to determine the offset.

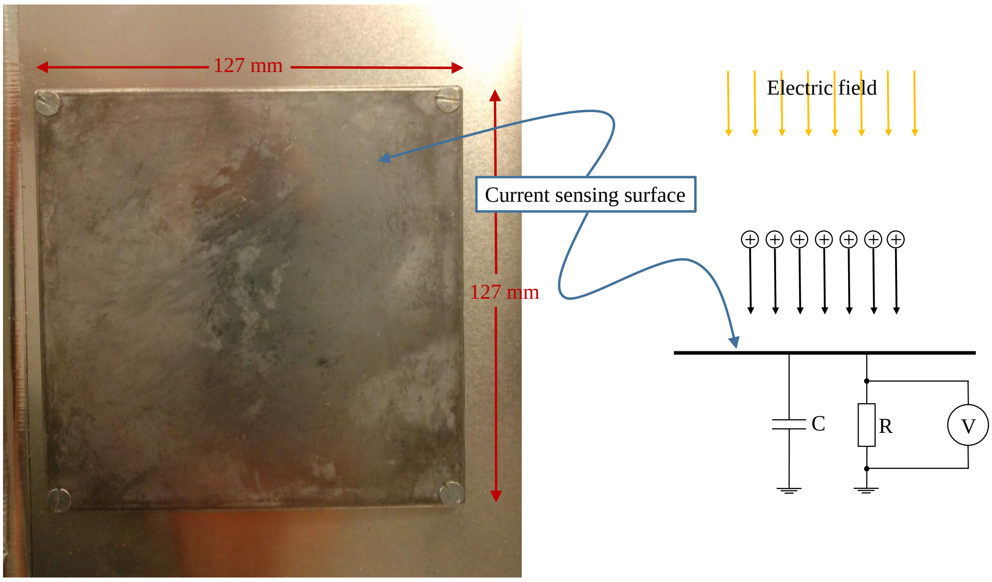

(a) **(b)**

Figure 3.4: **(a)** A photograph of the Wilson plate installed in the ion box, and **(b)** a schematic figure of a Wilson plate illustrating the working principle.

4

Experimental Setups

This chapter presents the different experimental setups utilized for this thesis work. Section 4.1 contains a collection of several indoor measurements at different locations. In Section 4.2 the setups for several outdoor and semi-outdoor measurements are described. Section 4.3 describes a high voltage environment with three different HV electrode configurations, and a humidifier. Finally. in Section 4.4 the setup for measurements both with and without applied voltage in the lab "Bastun" is described.

4.1 Indoor Measurements without Applied Voltage

Several indoor measurements were performed at different locations inside the CRC (Corporate Research Center) building in Västerås without applied voltage. The motivation was to investigate possible geographical and diurnal variations in ion concentrations. In Table 4.1 a compilation of the different measurement locations is presented. The first measurement was performed in Preparations lab, and the subsequent locations were chosen based on expected differences in radon radioactivity concentration. The floor number and the air ventilation schedule are provided in the table, since they are important parameters for radon concentration, and hence also for the ion concentrations. The ion box placement in one of the locations, the basement lab, is displayed in Fig. 4.1. In the figure one can observe that the ion box is placed on a table at a height of approximately 1 m above the floor. Furthermore, the placement is such that employees can walk by and affect the measurements, i.e. it is not an isolated measurement site. The setups in Preparations lab, Chemistry lab and in the conference room "Spänningen" look basically the same as the one in the basement lab (i.e. the ion box is placed on the same table) Therefore, photographs of the other setups are deemed redundant and are hence not included. Finally, environmental conditions are provided in the appendix, and the range setting for the air ion counters were 20,000 ions/cm^3.

Table 4.1: Floor number, air ventilation schedule and date for the different indoor ion box measurements.

Location	**Floor number relative to the ground floor**	**Time schedule for the air ventilation system**	**Date of measurement**
Preparations lab	One floor above the ground floor	On between 05:00 and 20:00 on weekdays, otherwise off	Between Wednesday 2017-03-15 and Monday 2017-03-20
Chemistry lab	One floor above the ground floor	On between 05:00 and 20:00 on weekdays, otherwise off	Between Tuesday 2017-03-21 and Monday 2017-03-27
Basement	One floor below the ground floor	On between 05:00 and 18:00 on weekdays, otherwise off	Between Wednesday 2017-03-29 and Monday 2017-04-03
Conference room "Spänningen"	Three floors above the ground floor	On between 05:00 and 20:00 on weekdays, otherwise off	Between Friday 2017-05-05 and Monday 2017-05-08

Figure 4.1: A photograph of the lab setup with the ion box in the basement lab, which is located one floor below the ground floor.

4.2 Outdoor and Semi-outdoor Measurements without Applied Voltage

Several outdoor and semi-outdoor measurements at different locations on the ABB Corporate Research property in Västerås, were performed without applied voltage. Semi-outdoor refers to measurements performed under a roof, in a storehouse with an open sectional door to the outside, see Fig. 4.2. In Table 4.2 a compilation of the different measurement locations is presented. As can be deduced from the table, the outdoor measurements (the locations are displayed in Fig. 4.3) were only performed during daytime, and not over night. The reason for this is that the ion box is not designed to withstand direct exposure to e.g. rain- or snowfall. Of course, some sort of cover could be designed for the ion box, in order to enable outdoor measurements, but such a cover was not constructed for this thesis work. Instead, semi-outdoor measurements in a storehouse were performed over several nights, since the storehouse roof protects the ion box from various weather conditions. It should be noted, however, that the roof also hinders the ground surface from being heated up due direct sunlight during the day. In turn, this can result in a discrepancy regarding ground exhalation of e.g. radon, and hence diurnal variations in the ion concentrations.

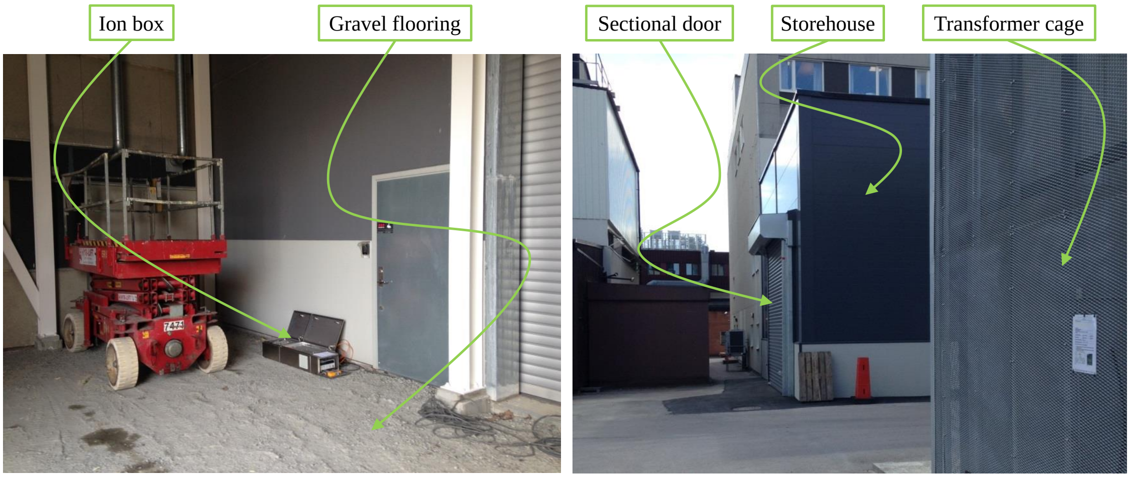

(a) **(b)**

Figure 4.2: **(a)** A photograph of the ion box placed on the gravel flooring inside the storehouse before the asphalt was laid, and **(b)** a photograph of the storehouse and the transformer cage from the outside.

Table 4.2: Locations and dates for the different outdoor and semi-outdoor ion box measurements.

Measurement	**Location**	**Date of measurement**
Outdoors 1	Inside one of the transformer cages	Between 13:03 and 16:05 on Tuesday 2017-04-11
Outdoors 2	Outside the transformer cages	Between 09:42 and 14:16 on Wednesday 2017-05-03
Semi-outdoors 1	The newly built storehouse (with gravel flooring)	Between Thursday 2017-04-13 and Tuesday 2017-04-18 (i.e. during the Easter holidays)
Semi-outdoors 2	The newly built storehouse (with asphalt flooring)	Between Friday 2017-04-28 and Wednesday 2017-05-03 (i.e. during the "Valborg" holidays)

In Fig. 4.3 the two different locations for the outdoor measurements are displayed, i.e. inside and outside of one of the transformer cages. The main reason for the choice of locations so close to each other, is the different flooring. In turn, the flooring could have an affect on the radiation emitted from the ground. Inside the cage, as displayed in Fig. 4.3 (a), the floor (and three walls) is made of concrete. In contrast, outside of the cage the ground has a layer of asphalt, as displayed in Fig. 4.3 (b). Furthermore, in Fig. 4.2 the location for the semi-outdoor measurements is displayed. The figure shows the newly built storehouse, in which measurements were performed first with the interim gravel flooring (Fig. 4.2 (a)), and thereafter when an asphalt layer had been laid. The sectional door visible in Fig. 4.2 (b) (the sectional door visible in the (a) figure is not the same) was supposed to be open during the measurements, but were sometimes closed anyway. Also visible in Fig. 4.2 (b) is the location of the transformer cage in relation to the storehouse. The distance between them is approximately 20 m. Finally, environmental conditions are provided in the appendix, and the range setting for the air ion counters were 20,000 ions/cm^3.

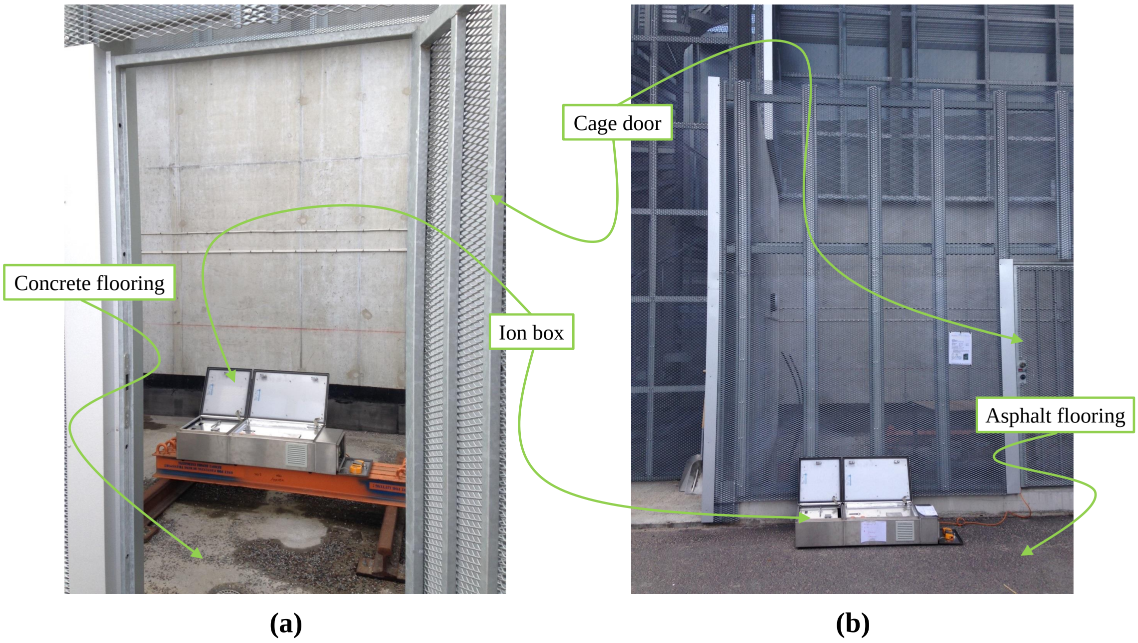

(a) **(b)**

Figure 4.3: **(a)** A photograph of the ion box placed inside one of the transformer cages, and **(b)** a photograph of the ion box placed just outside the same cage.

4.3 High Voltage Measurements in Small High Voltage Hall

In this section the lab setup utilized for the experiments performed in the small high voltage hall (SHVH) is described. Three variables were consciously altered during the measurements: applied DC high voltage, HV electrode shape, and relative humidity. Three different HV electrode configurations was used. The equipment utilized, i.e. the DC high voltage supply and humidifier are presented in Table 4.3. It should be emphasized that the digital display of the high voltage DC supply has a resolution of 1 kV, hence small steps in applied voltage are not very precise. Furthermore, the range setting for the air ion counters was 2,000,000 ions/cm^3. The general lab setup and the first HV electrode configuration, can be described by referring Fig. 4.4. The figure displays the ion box placed at the bottom of a grounded cylindrical cage under a HV sphere electrode. As one can deduce from the figure, the placement of the ion box is not symmetrical in the horizontal plane. Instead, the placement is such that the Wilson plate is close to the center of the cylinder, in order to achieve a more accurate reading of corona inception. Additional information that is provided from the figure are the dimension of the cage, and the location of the humidifier. The humidifier was used to together with a plastic cover around the cylindrical cage in order to artificially increase the relative humidity. The silicone rubber insulation that covers part of the connection between the HV DC supply and the HV electrode, is residual from a previous lab setup, and not a conscious design choice for this lab setup. However, one should be aware that it can affect the measurements.

Table 4.3: Instruments utilized in the small high voltage hall lab setup.

Manufacturer	**Product model**	**Description**
Glassman High Voltage, Inc.	Series LH	High voltage DC power supply
Hace	PCMH45	Humidifier

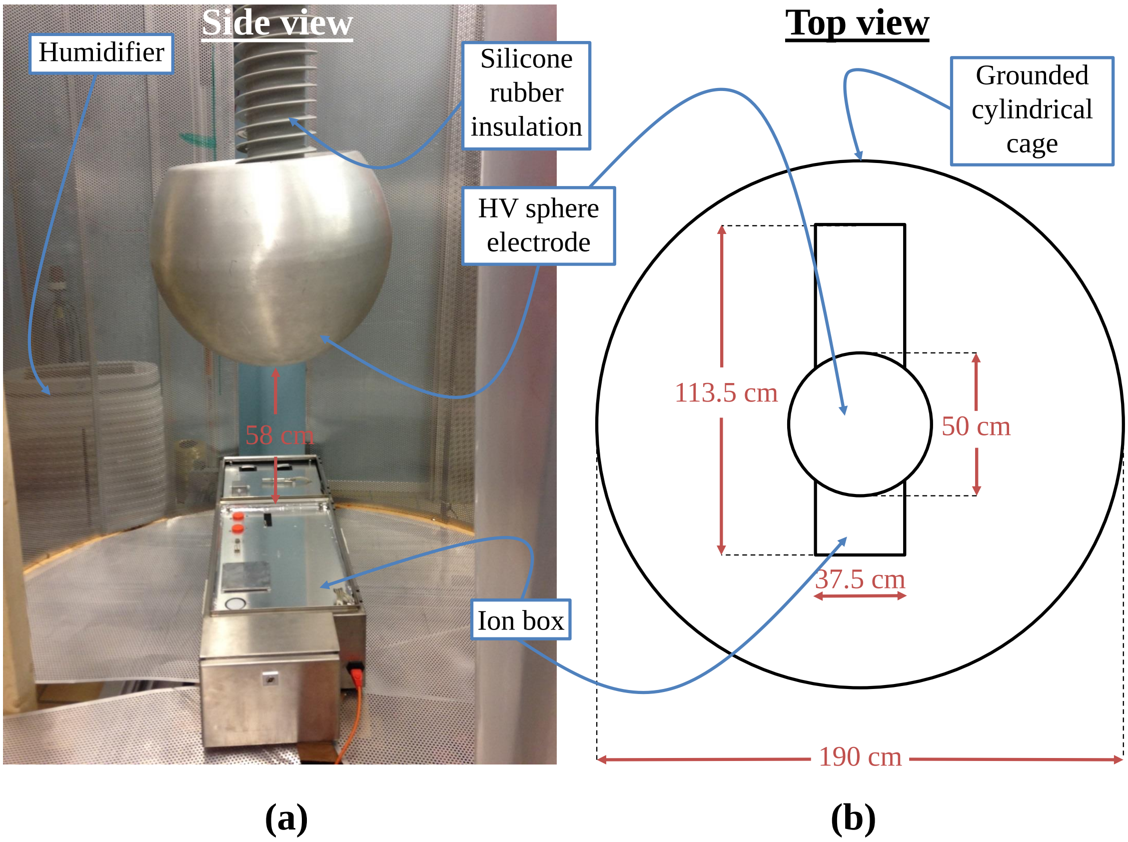

Figure 4.4: **(a)** A photograph of the lab setup with the ion box placed at the bottom of a cylindrical cage below a high voltage electrode, and **(b)** a top view sketch of the same lab setup.

A corona needle (i.e. a thin wire) was mounted on the sphere electrode in order to achieve a less uniform electric field distribution, and hence to facilitate corona discharges. In Fig. 4.5 this HV electrode configuration is displayed. Two different lengths of needles were utilized: 15 mm and 100 mm. The diameter of both needles were the same, but was however never measured. In order to further decrease the field uniformity, the sphere electrode was removed and a thinner corona needle replaced the previous one. In Fig. 4.6 this HV electrode configuration is displayed. As one can deduce from the figure, the diameter of the needle was roughly 0.1 mm, its length 30 mm, and the distance from the needle end point to the ion box 61 cm. Finally, in Table 4.4 the different high voltage measurements performed in the small high voltage hall are listed, and described in terms of electrode configuration and whether the humidifier was utilizied or not.

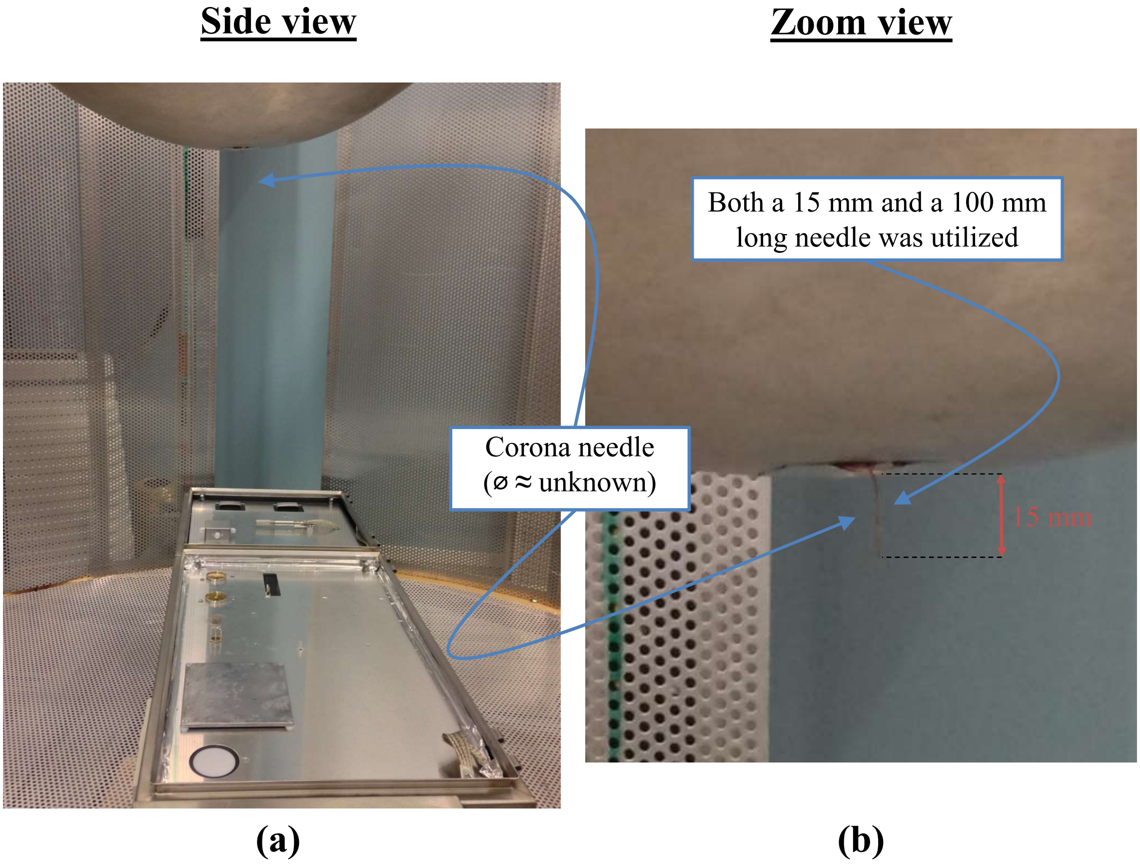

Figure 4.5: **(a)** A photograph of the lab setup with the thick corona needle mounted on the sphere electrode, and **(b)** a zoom view of the corona needle in the same setup. Apart from the different HV electrode, the lab setup is the same as displayed in Fig. 4.4.

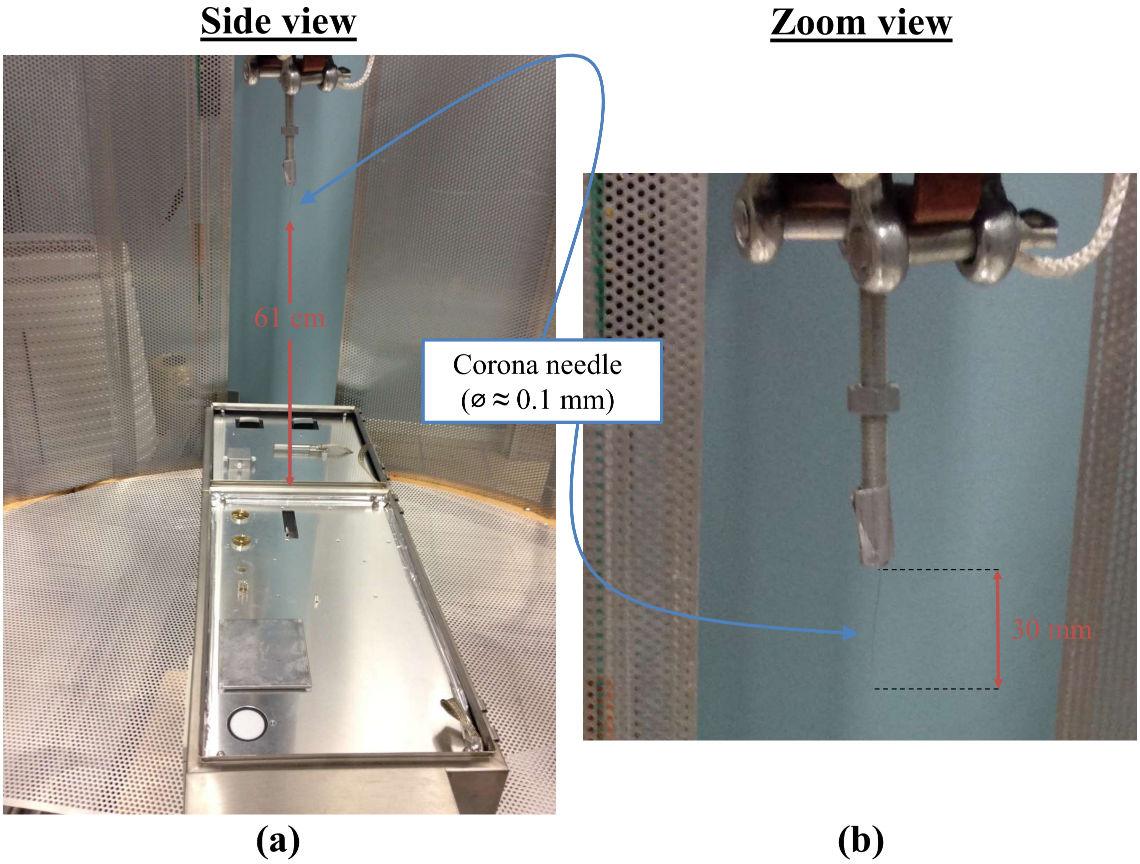

Figure 4.6: **(a)** A photograph of the lab setup with the thin corona needle without the sphere electrode, and **(b)** a zoom view of the corona needle in the same setup. Apart from the different HV electrode, the lab setup is the same as displayed in Fig. 4.4.

Table 4.4: Description of the different high voltage measurements performed in the small high voltage hall.

Measurement	HV Electrode configuration	Description	Date of measurement
SHVH 2	Sphere	Humidifier was ON	Thursday 2017-02-16
SHVH 3	Sphere	Humidifier was OFF	Thursday 2017-02-16
SHVH 4	15 mm corona needle (Ø $>$ 0.1 mm) attached to sphere	Humidifier was OFF	Tuesday 2017-02-21
SHVH 5	100 mm corona needle (Ø $>$ 0.1 mm) attached to sphere	Humidifier was OFF	Tuesday 2017-02-21
SHVH 7	30 mm corona needle (Ø $=$ 0.1 mm) without sphere	Humidifier was OFF	Tuesday 2017-02-21

4.4 Measurements in "Bastun"

In this section the lab setup utilized for the experiments performed in the lab "Bastun" is described. The following parameters were consciously altered during the measurements: applied DC voltage polarity and amplitude, HV electrode shape, humidity and heat. The equipment utilized, i.e. the DC high voltage supplies and humidifier are presented in Table 4.5. As can be deduced from the table, two different DC high voltage supplies were used, one for positive voltage and another for negative voltage. The digital display of the high voltage DC supplies both has a resolution of 0.1 kV. The humidifier is the same one utilized for the measurements in the small high voltage hall. Finally, the range setting utilized for the air ion counters was 20,000 ions/cm^3.

The general lab setup can be described by referring to Fig. 4.7. The figure displays the ion box placed inside a sealed chamber located in the lab "Bastun". The chamber is equipped with a heating system, which is controlled from the outside of the chamber, by providing a specific setpoint value for the temperature. Heated air is then blown into the chamber through the pipes and valves that runs along the long sides of the chamber, as displayed in the figure. The air leaves the chamber through two valves located in the roof, where it is re-heated and passes through a closed system of pipes, and back into the chamber. Above the ion box is a HV toroid electrode, which is tied with textile tape to a wood structure. The horizontal placement of the toroid is such that its center projection on the ion box is located in between the air ion counters and the field mills. The HV supplies are located and controlled from outside of the chamber. Additional information that is provided by the figure are the dimensions of the chamber, the locations of the humidifier and heating system pipes. In addition to HV measurements performed with the toroid electrode, measurements were also done with a corona needle (a piece of wire) attached on the bottom center of toroid. This electrode configuration is displayed in Fig. 4.8, where it can be observed that the diameter of the needle was 1 mm, while the length of the needle was 18.5 cm. The distance between the corona needle point and the ion box were hence 41.5 cm.

Table 4.5: Instruments utilized in the "Bastun" lab setup.

Manufacturer	Product model	Description
Spellman	SL100P150	Positive high voltage DC power supply (max. + 100 kV DC)
Spellman	SL100PN150	Negative high voltage DC power supply (max. - 100 kV DC)
Hace	PCMH45	Humidifier

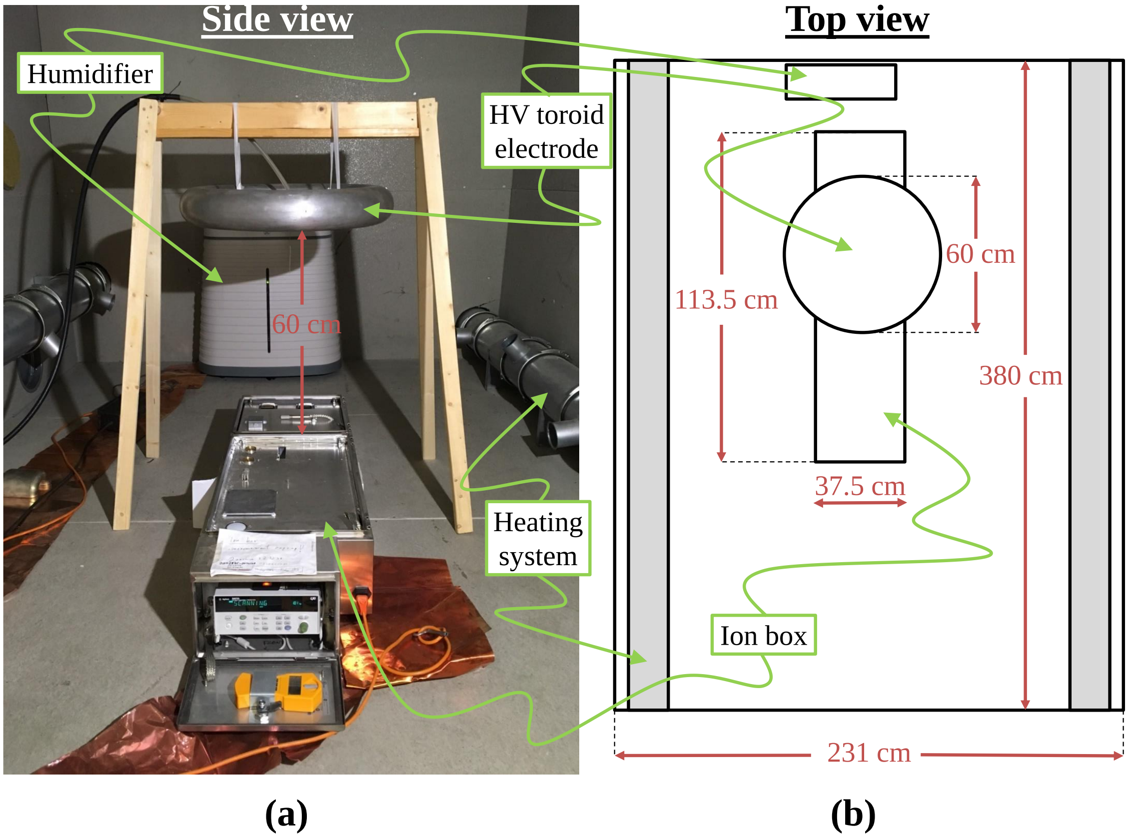

Figure 4.7: **(a)** A photograph of the lab setup with the ion box placed in the lab "Bastun", below a high voltage electrode, and **(b)** a top view sketch of the same lab setup.

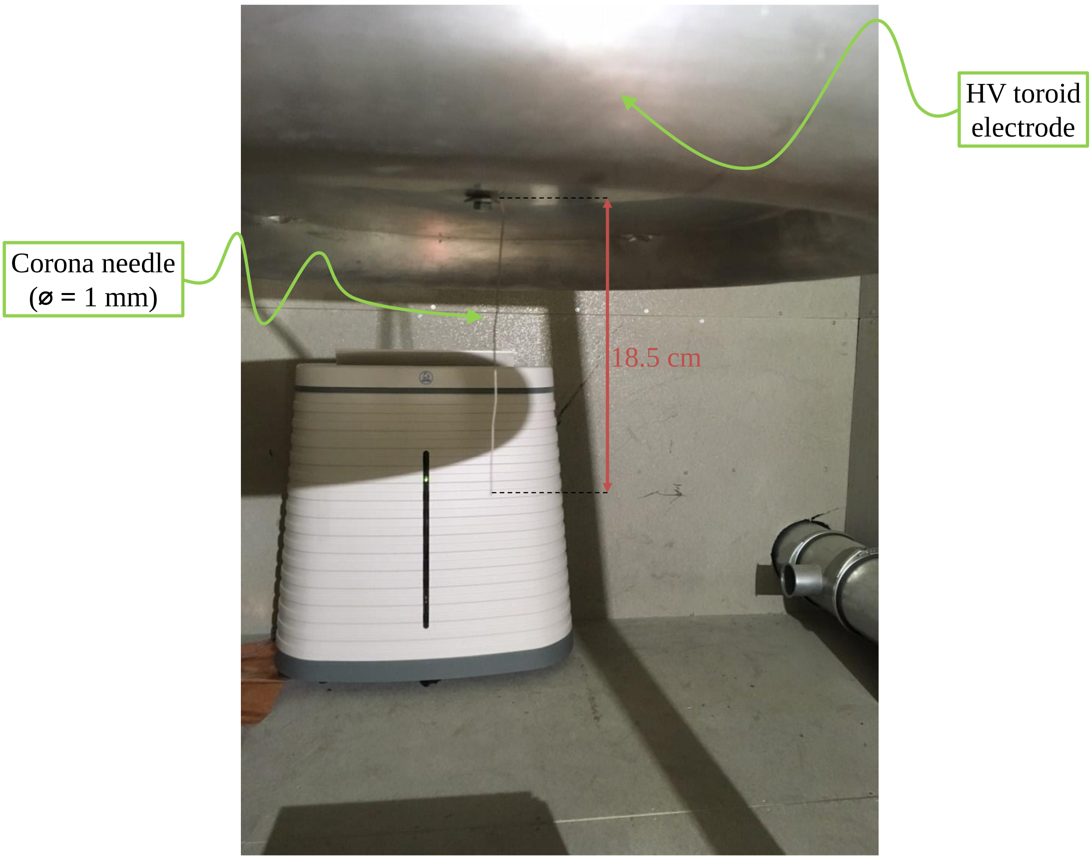

Figure 4.8: A zoom view photograph of the corona needle mounted on the HV toroid electrode.

Measurements both with and without applied voltage were performed in "Bastun". In Table 4.6 the different equilibrium measurements are listed with dates, and described in terms of whether the humidifier and heating system were on or off. Similarly, in Table 4.7 the high voltage measurements are described regarding electrode configuration, and whether the heating system and humidifier was on during the measurements.

Table 4.6: Description of the different equilibrium measurements performed in the lab "Bastun".

Measurement	**Description**	**Date of measurement**
Bastu 1	Both humidifier and heat were OFF	Between Wednesday 2017-05-10 and Friday 2017-05-12
Bastu 3	Humidifier was ON (high fan speed and continuous on the humidity setting) and heat was OFF	Between Friday 2017-05-12 and Monday 2017-05-15
Bastu 8	Humidifier was OFF and heat was ON (setpoint 40 °C)	Between Tuesday 2017-05-16 and Wednesday 2017-05-17
Bastu 11	Humidifier was ON (high fan speed and continuous on the humidity setting) and heat was ON (setpoint 40 °C)	Between Wednesday 2017-05-17 and Thursday 2017-05-18
Bastu 13	Humidifier was ON (high fan speed and continuous on the humidity setting) and heat was OFF (but ON initially until the temperature reached 40 °C)	Between Friday 2017-05-19 and Monday 2017-05-22

Table 4.7: Description of the different high voltage measurements performed in the lab "Bastun".

Measurement	**HV Electrode configuration**	**Description**	**Date of measurement**
Bastu 7	Toroid	Humidifier was ON (low fan speed), and heat was OFF	Tuesday 2017-05-16
Bastu 8	Toroid	Humidifier was OFF, and heat (40 °C) had been ON before	Wednesday 2017-05-17
Bastu 10	Corona needle attached to toroid	Both humidifier and heat were OFF	Wednesday 2017-05-17
Bastu 11	Corona needle attached to toroid	Both humidifier and heat (40 °C) had been ON before	Thursday 2017-05-18
Bastu 12	Toroid	Humidifier was ON (high fan speed), and heat (40 °C) had been ON before	Thursday 2017-05-18

5

Presentation and Analysis of Measurement Data

In this chapter measurement data obtained from the different lab setups described in Chapter 4 are presented, analysed and discussed. In addition, offset values, and equations for calculations of both ion concentration and conductivity are presented. Post-processing of measurement data was performed in Igor Pro 7.02 64-bit version, for which a so-called procedure (a software routine) was programmed. The procedure contains a graphical interface where one can choose to load and plot measurement data from the Agilent DAQ unit, Radon Monitor R1, and Gamma-Scout Geiger counter. Additionally, the procedure calculates ion concentration from the measured radon radioactivity concentration, and conductivities from both measured ion and radon radioactivity concentrations.

5.1 Offset Adjust

In this section the results from the offset adjust methods described in Chapter 3 are presented. For the air ion counters the offset calibration should be performed by averaging the ion concentration signals during the fan turn-off time (during which the concentrations ideally should be zero). However, there are some problems with this method. First of all, the negative ion counter is quite noisy, which means that several calibration occasions must be averaged in order to calculate a representative average value. Secondly, for at least the positive ion counter there seems to be a correlation between measured equilibrium concentration and offset value. This can be observed in Table 5.1 where four different calibration values for each air ion counter are presented. In the table, the averaged positive ion concentration value during calibration decreases as the equilibrium ion concentration increases. For the negative ion counter the same trend is not observed. Due to these conflicting calibration values, no offset adjust is utilized for the ion concentration data presented in this thesis. Instead, Table 5.1 can be used as a reference of the offset values at some different equilibrium concentrations.

Table 5.1: Calibration of the air ion counters during different measured equilibrium ion concentrations. The averaged value during calibration is the average of 15 subsequent calibration occasions.

Air ion counter	**Measurement**	**Equlibrium concentration** [**ions/cm^3**]	**Averaged offset value during calibration** [**ions/cm^3**]	**Offset in percentage of equilibrium concentration** [%]
Positive	Chemistry lab (daytime steady-state during a weekday)	660.6	17.1	+2.6
Positive	Chemistry lab (during a weekend)	2379.6	-6.3	-0.3
Positive	Bastu 1	2910.1	-32.7	-1.1
Positive	Basement lab	4618.3	-73.8	-1.6
Negative	Chemistry lab (daytime steady-state during a weekday)	-551.3	-24.2	+4.4
Negative	Chemistry lab (during a weekend)	-2187.4	-5.5	+0.25
Negative	Bastu 1	-2378.9	-25.0	+1.1
Negative	Basement lab	-3819.9	-24.5	+0.6

Determination of the offset values for the ion current measured with the Wilson plate, and the electric field strength measured with the field mills, were performed in the following way. For the Wilson plate, measurements were performed with the lids of the ion box closed. Since the lids are grounded, the measured current should be zero. Similarly, for the fields mills, measurements were performed with the small grounded caps attached on top of instruments. The average values of two separate 3 min measurements were determined, and is presented in Table 5.2. For reference, the average temperature during the measurements were 23.6 and 22.8 °C respectively.

Table 5.2: Offset values utilized for offset adjust of the data presented in this thesis.

Measurement	**Offset value**
Air ion counter set to measure positive ions	0 [ions/cm^3]
Air ion counter set to measure negative ions	0 [ions/cm^3]
Field mill 1 (200 kV/m range)	-0.00109 [kV/mm]
Field mill 2 (5 kV/m range)	0.0000978 [kV/mm]
Ion current (Wilson plate, 100 nA range)	-22.9 [pA]
Ion current (Wilson plate, 1 nA range)	-30.7 [pA]

5.2 Calculations

In the following text the calculations performed during the post-processing of the measurement data is presented. The small ion concentration due to Rn-222 radioactivity are calculated using (2.11) and (2.9), which for sake of convenience are displayed here again

$$n = \sqrt{\frac{q}{\alpha}} = \sqrt{\frac{q_{Rn-222}}{1.5 \cdot 10^{-6}\ \mathrm{s^{-1}m^{-3}}}} \tag{5.1}$$

where n is the small ion concentration [$\mathrm{m^{-3}}$], $\alpha = 1.5{\cdot}10^{-12}\ \mathrm{s^{-1}m^{-3}}$ is a literature value for the ion-ion recombination coefficient (obtained from Table 2.3), and q_{Rn-222} is the ionization rate [$\mathrm{s^{-1}m^{-3}}$] due to Rn-222 radioactivity and is calculated as

$$q_{Rn-222} = 1.5684 \cdot 10^{5}\ \text{ion pair} \cdot (\text{radon radioactivity concentration}) \tag{5.2}$$

The conductivity is calculated using (2.13), which is also displayed here again for sake of convenience

$$\sigma = \sigma_{+} + \sigma_{-} = e\left(\sum_i \mu_i^{+} n_i^{+} + \sum_i \mu_i^{-} n_i^{-}\right) \tag{5.3}$$

which in turn reduces to the following equation, since only small ions are taken into consideration

$$\sigma = e\mu^{\pm}(n^{+} + n^{-}) = 1.6023 \cdot 10^{-19}\ \mathrm{C} \cdot 1.6 \cdot 10^{-4}\ \mathrm{m^2/Vs}\ (n^{+} + n^{-}) \tag{5.4}$$

where $e = 1.6023{\cdot}10^{-19}$ C is the elementary charge, $\mu^{\pm} = 1.6{\cdot}10^{-4}\ \mathrm{m^2/Vs}$ is an average small ion mobility value from literature [10], and n is the small ion concentration [$\mathrm{m^{-3}}$].

5.3 Diurnal Variations in Ion Concentrations

In order to analyse the diurnal variations in ion concentrations from the measurements described in Chapter 4, ion and radon radioactivity concentrations are plotted versus time. In Fig. 5.1 data from measurements performed in Chemistry lab is displayed. In the figure, positive ion concentration (red dots, using the left vertical axis), negative ion concentration (blue dots, using the left vertical axis), and the radon radioactivity concentrations (green lines with markers, using the right vertical axis) are plotted. For convenience, positive ions are shown as positive values and negative ions are shown as negative values. In addition, a smoothed radon radioactivity curve (black line, using the right vertical axis) is also plotted in order to facilitate analysis. Smoothing is a type of signal processing in Igor Pro which filters out short-term variations. The annotations with arrows in the figures corresponds to the time schedule for the ventilation system (see Table 4.1), and are displayed in order to facilitate analysis of diurnal variations in ion concentrations indoors. In Fig. 5.1 one can observe that the fluctuations in ion concentrations during the weekdays are matched by similar fluctuations in the radon radioactivity concentrations. In turn, these fluctuations seems to correlate well with the time schedule for the ventilation system, i.e. when the ventilation is turned on at 05:00 the concentrations of both ions and radioactivity are reduced. During the times when the air ventilation is on, the air born gas radon is not able to accumulate in the room, hence the ionization rate due to radon is reduced. In addition, the increased air flow due to the air ventilation might promote increase in ion-ion recombination rate, i.e. further contributing to lower ion concentrations. In contrast, when the ventilation is turned off at 20:00 the concentrations increase. This can be explained by radon's tendency to accumulate when the air ventilation is off, which in turn provides a higher ionization rate. Corresponding figures for the other measurements are provided in the Appendix.

Utilizing the formulas provided in Section 5.2, the ion concentration due to radon radioactivity can be calculated. In Fig. 5.2 the measured (red and blue dots) and calculated (black lines with markers) ion concentrations are plotted, from measurements performed in Chemistry lab. In addition, a smoothed curve of the calculated ion concentration (green lines with markers) is also plotted. In order to facilitate analysis of the negative ion concentration, the curves for the calculated ions are also mirrored (multiplied with -1) on the other side of the zero line. Although radon is considered the major source of ionization, other sources contributes as well. These sources include cosmic radiation, radiation emitted from the ground, and radon daughters. Hence, the curve representing calculated ions in Fig. 5.2 should ideally underestimate the measured ions. In the figure one can observe that during the weekend the calculated ions underestimate the measured positive ions. The measured negative concentration generally lower than the positive concentration. A ratio 1.12 between positive and negative ions is to be expected due to the electrode effect [17]. However, during the weekdays the calculated ion concentration instead overestimates the measured concentrations. Furthermore, the discrepancy is the largest during daytime when the air ventilation is on. This suggests that not only does the air ventilation promote lower ionization rate because of lower radon concentration, but also an increase in deionization processes.

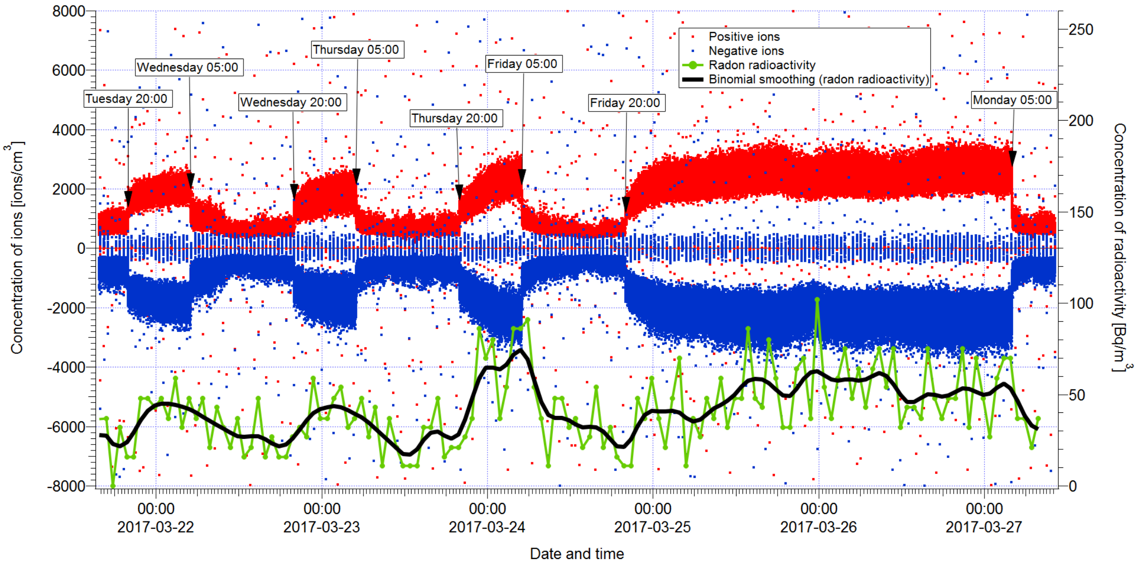

Figure 5.1: Concentrations of ions and radon radioactivity plotted versus time, from the measurements in Chemistry lab.

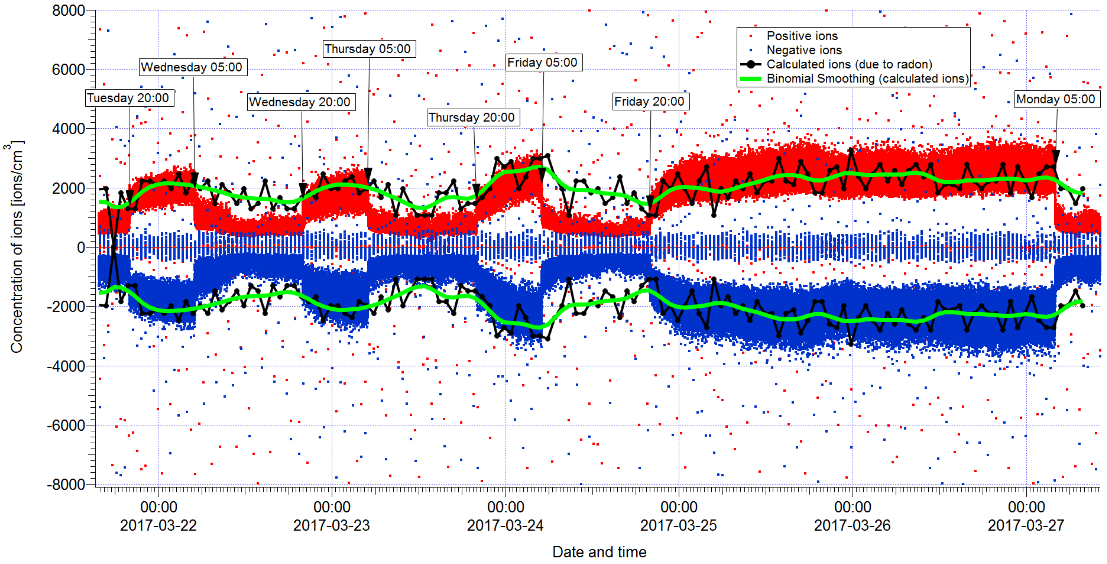

Figure 5.2: Measured and calculated concentrations of ions plotted versus time, from the measurements in Chemistry lab.

In Fig. 5.3 calculated conductivity using both measured ion concentrations (red dots) and radon radioactivity (black line with markers) are plotted. The data is from the measurements performed in Chemistry lab. In addition, smoothed curves are also plotted. Since the calculations are based on the measured ion and radon concentrations respectively, the same diurnal variations have propagated into the conductivity. Similarly, the discrepancy between measured and calculated ion concentrations displayed in Fig. 5.2 have also propagated into the conductivity curves plotted in Fig. 5.3.

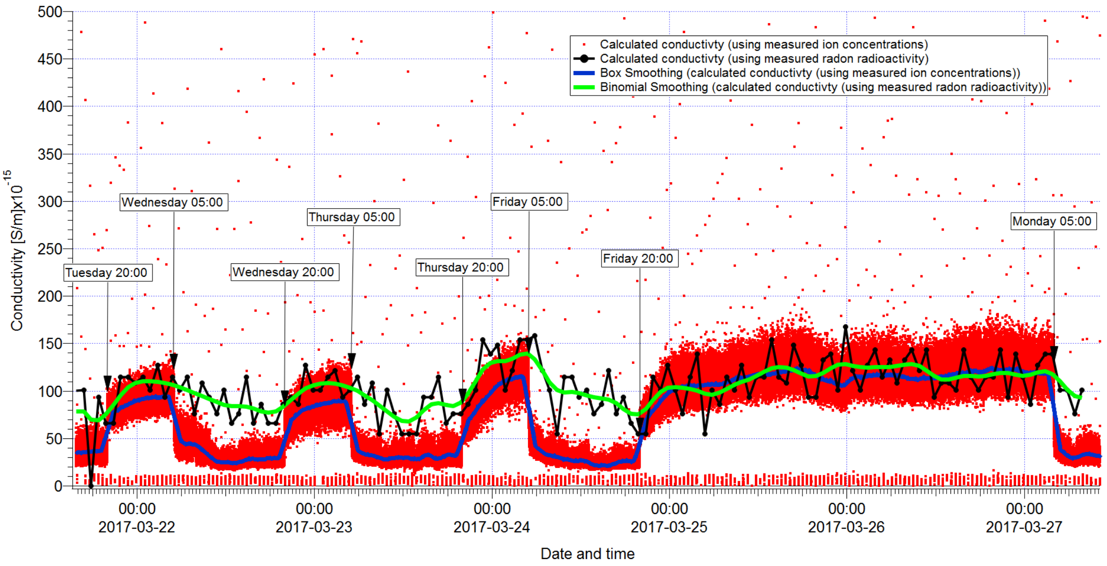

Figure 5.3: Calculated conductivity of air plotted versus time, from the measurements in Chemistry lab.

5.4 Equilibrium Ion Concentrations

In order to analyse and compare the equilibrium ion concentrations from the measurements described in Chapter 4, several category plots are presented (see also the appendix where measured and calculated values are provided in tables). The category plots display averaged data of different ion concentration related quantities. In Fig. 5.4 the indoor measurements described in Section 4.1 are compared. The different measurement locations are presented on the horizontal axis. For the measurements in Preparations lab and Chemistry lab, two different levels of ion concentration equilibrium were reached. One high level during the weekends (together with late nights and early mornings), and a low level during daytime. The reason for this is the time schedule of the air ventilation, as described in Section 5.3. In Fig. 5.4 positive, negative and calculated ion concentrations are represented by red, blue and yellow bars respectively, and their amplitudes correspond to the first left vertical axis. The green bars represent radon radioactivity and correspond the first right vertical axis. The black bars represent conductivity (calculated using the measured ion concentrations) and correspond to the second left vertical axis. The turquoise bars represent gamma radiation and correspond the second right vertical axis.

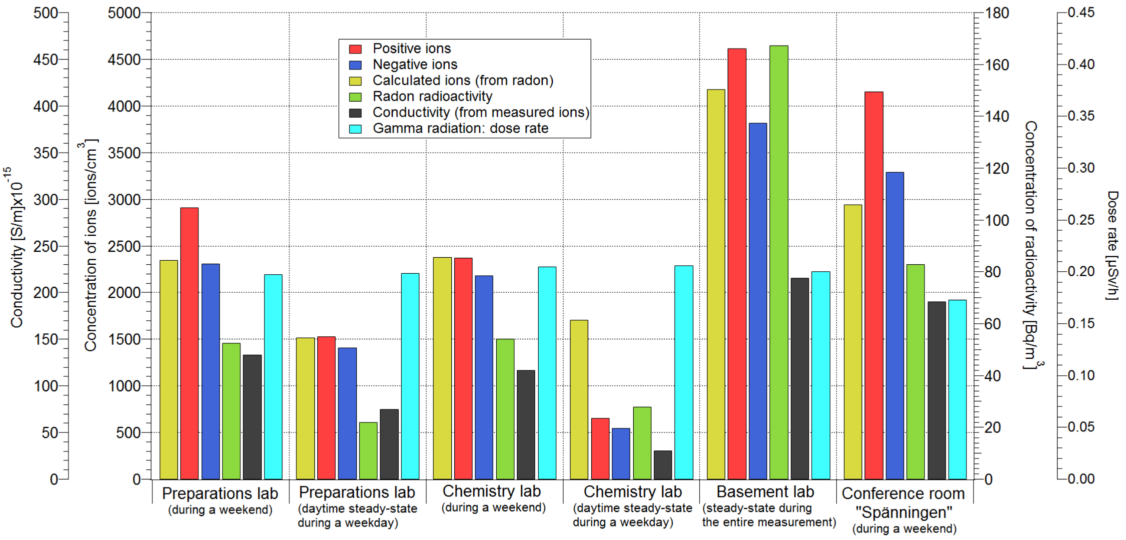

Figure 5.4: Category plot displaying equilibrium values at different indoor locations.

Since the Chemistry lab measurements are analysed in Section 5.3, they can serve as reference for analysing the remaining locations in Fig. 5.4. By comparing the weekend equilibrium concentrations in Preparations lab and Chemistry lab, one can observe that there are significantly more positive ions in Preparations lab. Although, both the negative ion concentration and the radon concentration is very similar for both locations. A possible explanation for the larger ratio of positive ions in Preparations lab can be that the air is not as well mixed during the weekend as it is in Chemistry lab, which has several fume cupboards. Another possible explanation for the larger ratio of positive ions in Preparations lab can be weak static electric fields created by e.g. plastic materials in the vicinity of the ion box. Furthermore, the ratio between calculated ions due to radon and measured positive ions also differ between the locations. Generally the ratio is higher when the air ventilation is on during the weekdays. This suggests that the air ventilation system induces either an decrease in ionization rate from other sources than radon, or an increase in deionization rate. The decrease in ionization rate can be accomplished if the ration between radon and its daughter is increased when the air ventilation system is on, i.e. if the radon daughters are more easily ventilated out of a room. The increase in deionization rate can be accomplished if the air flow caused by the air ventilation e.g. promotes ion-ion recombination.

Both the largest ion concentrations and radon radioactivity concentrations are found in the basement lab, as displayed in Fig. 5.4. This is most likely due to radon entering the building from the ground through cracks and crevices in the basement floor. More peculiar is the almost as high concentrations of ions in the conference room "Spänningen", which is located on the third floor of the building. Although the radon concentration is higher there than in both Preparations lab and Chemistry lab, it is still only half of the value in the Basement lab. This is also the location where the discrepancy between measured positive ions and calculated ions due to radon is the largest. One possible explanation is that since the room is by far the smallest of them all, the air in there is the most still and hence the rate of deionization by ion-ion recombination might be lower. Which in turn allows for larger equilibrium ion concentrations. Another difference between "Spänningen" and the other locations that is worth mentioning, is that "Spänningen" is the only location with a fitted carpet. Finally, the measured gamma radiation is very similar for all indoor locations.

In Fig. 5.5 the different outdoor and semi-outdoor measurements described in Section 4.2 are compared. For reference, the measurements from Chemistry lab are also included in the figure. Starting with the measurements denoted Outdoors 1 and 2, one can observe that they are very similar, except for the gamma radiation. The discrepancy can be explained by the concrete flooring at the Outdoors 1 location, which can screen gamma radiation. Whereas Outdoors 2 has asphalt flooring. The similar levels of ions and radon are reasonable since the measurement locations are so close to each other. Furthermore, the lower levels of radon at Outdoor 1 and 2 compared to the measurement in Chemistry lab during the weekend explains the lower ion concentrations. However, comparing Outdoors 1 and 2 with Chemistry lab during the a weekday, one can observe that ion concentrations are higher outdoors, while the radon concentrations are lower. This suggest a difference between how typical windy conditions outdoors and air ventilation indoors affect ion and radon concentrations. One should be aware though that the measurements outdoors were only performed for a few hours.

By comparing equilibrium values for the measurements denoted Semi-outdoors 1 and 2 in Fig. 5.5, one can notice the rather large difference in ion concentrations. Although the two measurements were performed in the same storehouse, but the ion box placement inside were not the same. Furthermore, the flooring were different, and the measurements took place 2 weeks apart. The discrepancy between Semi-outdoors 1 and 2 is not easily understood, but some possible explanations are listed in the following text. The weather during Easter could have been more favorable for higher ion concentrations, e.g. by less turbulent air flow, which in turn could mean less deionization by ion-ion recombination. The gravel flooring surface in Semi-outdoors 1 could either better promote ionizing radiation emitted from the ground, or contain a higher concentration of deposited radon daughters. However, this is partly contradicted by the higher levels of gamma radiation measured in Semi-outdoors 2, which probably is due to the asphalt containing uranium.

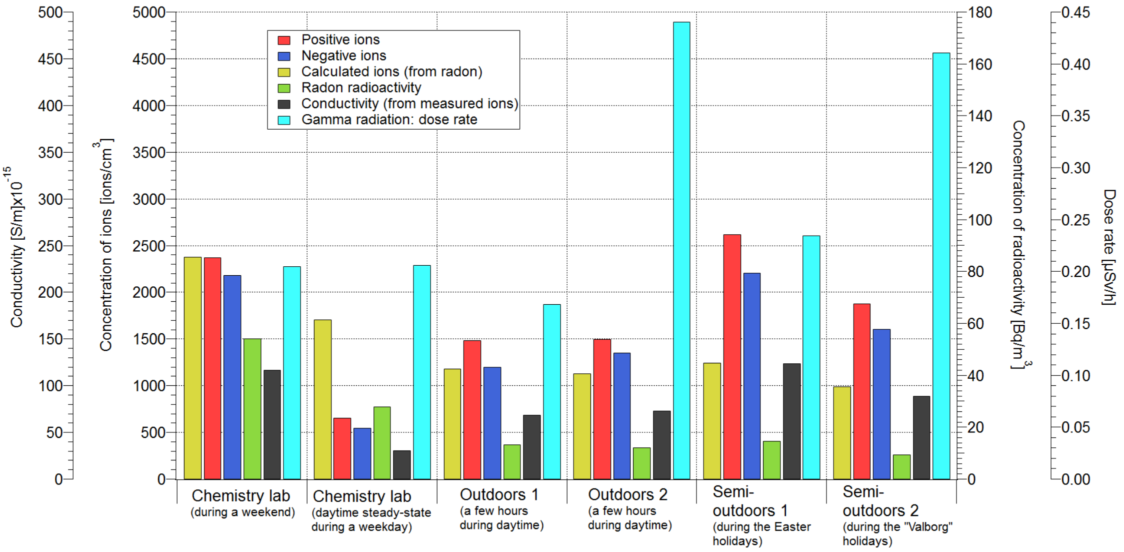

Figure 5.5: Category plot for equilibrium values at different outdoor and semi-outdoor locations.

In Fig. 5.6 the different measurements performed without voltage in the lab "Bastun", described in Section 4.4 are compared. There are two main differences between this category plot and the previous two. One difference is that the range of the vertical axis for concentration of ions is increased to maximum 17,000 ions/cm^3. The other difference is that bars for absolute humidity is included (purple bars corresponding to third vertical axis to the right). The Bastu 1 measurement was performed without any additional heat or humidity, and can hence be used as reference. The concentrations of both ions and radon is similar to the levels measured in Preparations lab during a weekend, see Fig. 5.4. Although the calculated ions in Bastu 1 underestimates the positive ions more than in Preparations lab. Which can be related to the smaller volume of the lab "Bastun" and the different materials of the surrounding walls, floor and roof. By comparing Bastu 1 with the Bastu 3 measurements (in which the humidifier was turned on), one can deduce that the negative ion concentration more than doubles after the humidifier has been on for 23 h. However, the positive ion concentration instead decrease. Furthermore, after 39 h the negative ion concentration has increased to more than five times the concentration measured in Bastu 1, even though the absolute humidity does not increase significantly from the measurement after 23 h to the measurement after 39 h. This illustrates that it can take a long time for the negative ion concentration to increase due to high humidity levels. There can be several explanations for the correlation between high humidity and high negative ion concentration. One theory is that the positive ions create larger clusters with the water vapor molecules, hence lowering the concentration of small positive ions. In turn, this creates less opportunities for the negative ions to recombine with positive ions, and hence the concentration of negative ions can increase. Another possible explanation is that it instead is the humidifier itself that creates negative ions as it injects water vapor into the air.

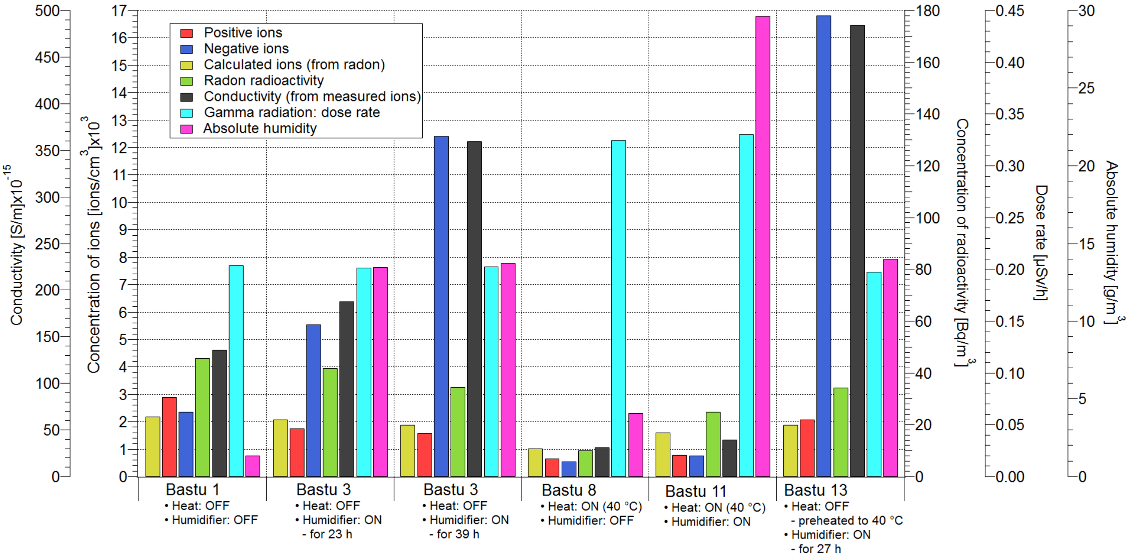

Figure 5.6: Category plot containing equilibrium values from the different measurements performed in the lab "Bastun".

In the Bastu 8 measurement presented in Fig. 5.6, the setpoint value of the heating system was 40 °C. As can be observed in the figure, the ion and radon concentrations are suppressed significantly, similar to what was observed when the air ventilation system was on in Preparations lab and Chemistry lab (see Fig. 5.4). This suggests that it is the forced air flow, and not the heat that is the main cause of the low ion concentrations. Another interesting observation is that the measured gamma radiation increase with around 60 % when the heating system is on. It is probably not the measuring device malfunctioning due to the increased temperature, since the Gamma-Scout instrument has a rated operating temperature up to 60 °C. Hence, the cause of the increase in gamma radiation is unknown, but could be related to an eventual increase in deionization. Or it could be that the forced air flow distributes gamma-ray emitting particles in a more favorable position in relation to the Geiger counter. In the Bastu 11 measurement both the heating system and the humidifier is on. The idea was that the higher temperature would allow for a larger concentration of water molecules in the air. Although the absolute humidity is pushed up to really high values, the ion concentrations remain at similar small levels as in Bastu 8. This suggests that air flow is probably the most important parameter considering equilibrium ion concentrations. In the last measurement, i.e. Bastu 13, the idea was to initially heat up the chamber to 40 °C, and then turn off the heating system. However, the temperature dropped faster than anticipated, but still the absolute humidity was increased a little beyond the levels in Bastu 3. The negative ion concentration in Bastu 13 reached a maximum steady-state level of 16,800 ions/cm^3, i.e. more than 7 times the negative concentration in Bastu 1. It is hard to say whether the small difference in absolute humidity between Bastu 13 and Bastu 3, is enough to account for the large difference (+35 %) in negative ion concentrations, or if there are other differentiating factors.

5.5 Ion Sweep-out and Relaxation due to Applied Voltage

In order to illustrate the effects of sweep-out and relaxation of ions, ion concentrations (red and blue dots, using the left vertical axis), DC electric field strength at ground potential (black curve, using the first vertical axis on the right side) and ion current (green curve, using the second vertical axis on the right side) are plotted versus time in Fig. 5.7. The data is from the measurement SHVH 3, which is described in section 4.3. In addition, annotations with arrows in the figure indicate the voltages applied, using the plateaus in DC field as reference. It should be stressed that the black curve is DC field strength, and not voltage. The annotations that reads calibration of air ion counters indicate that the ion measurement is turned off for one minute, and that the signal from the air ion counters reaches max. during the transient on/off periods. From the figure one can deduce that as the voltage first is stepped to +2.5 kV, the ion concentrations are reduced significantly, i.e. most of the ions are swept out. As the voltage is stepped to 5 kV, the concentrations are swept out even more. The relaxation process occurs when the applied voltage is switched off (e.g. from 5 kV to 0 V in the figure) and the ion concentration returns to equilibrium, and is governed by the ion generation rate which is mostly due to radioactive decay of radon. One can also observe how the measured ion current does not increase as the voltage is stepped from 25 to 50 kV, i.e. it is in the sweep-out region (see Fig. 2.2). However, it should be noted that the current measurement is not very sensitive, and may hence not be accurate in the pA range.

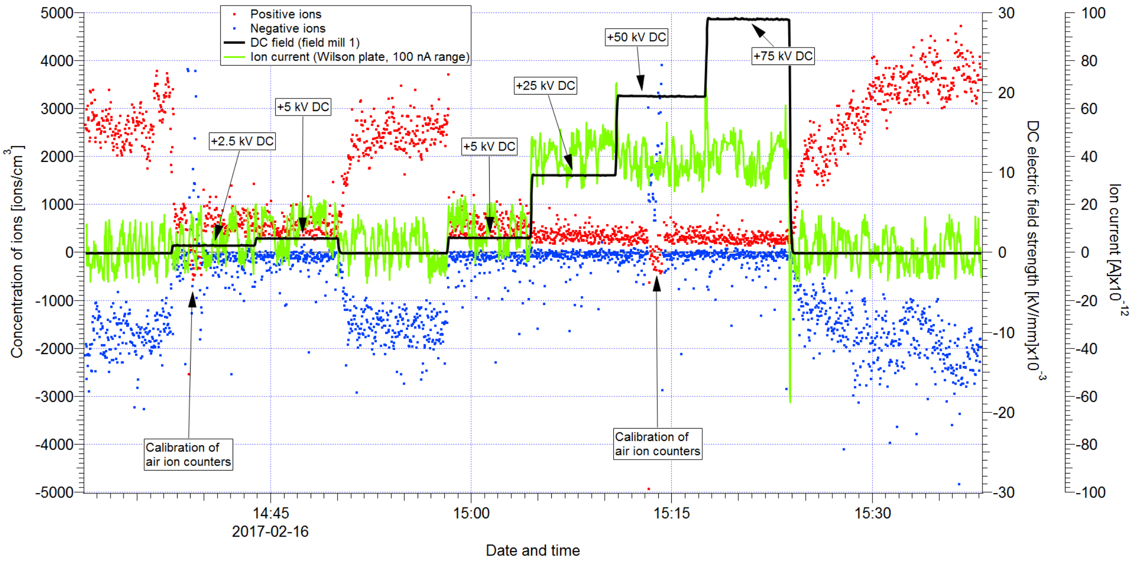

Figure 5.7: Ion concentrations, DC electric field strength, and ion current plotted versus time, from the measurement SHVH 3.

In order to further analyse the sweep-out and relaxation effects of air ions, piecewise averaging (turqoise and green horizontal lines) and exponential curve fitting (turqoise and green dashed curves) of the ion concentrations are presented in Fig. 5.8. Annotations with arrows in the figure indicate average ion concentrations, and time constants for the exponential curve fits of the relaxation process. In the figure one can observe that the average value of positive ion concentration decrease more as the applied voltage is increased. The negative ion concentration behave somewhat different. First of all, they decrease to lower concentrations faster, and they seem to reach minimum levels already at +25 kV. This can be explained by considering that the ion counters measures the concentration at ground potential, and the applied DC voltage is positive. Hence negative ions are accelerated away from the ion box, whereas positive ions are accelerated towards it. In turn, due to the non-uniform electric field distribution, this means that concentration of positive ions will increase with distance towards the ground electrode, and vice versa for the negative ion concentration. Also worth noting is that the initial equilibrium ratio between positive and negative ions is quite large, i.e. 1.45. This could e.g. be related to the plastic around the grounded cage. Another observation is that both ion concentrations reach higher values after step down from +75 kV to 0 V. The reason for this is unknown, but similar observations have been made in other measurements.

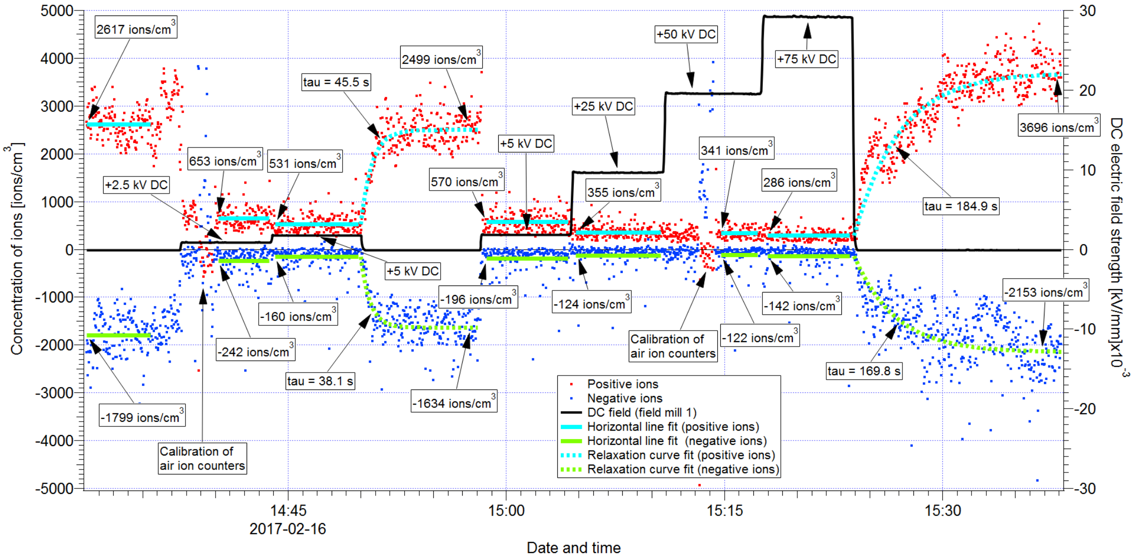

Figure 5.8: Ion concentrations with piecewise averaging and curve fitting, and DC electric field strength versus time, from the measurement SHVH 3.

5.6 Ion Injection due to Corona Discharges

In order to analyse the behavior of air ions during corona discharges, two graphs containing data from two of the different corona needle setups described in Chapter 4 are presented here. The first graph, Fig. 5.9 contains data from the measurement Bastu 10. In this figure the ion concentrations are plotted as red and blue lines, instead of dots as in previous graphs. In the figure it can be observed that the positive ion counter registers the corona induced ion current when the applied voltage is stepped from 15 kV to 16 kV. In contrast, the negative ion counter registers an ion current already the first negative voltage step from 0 V to -14 kV. Since both ion counters were set to the lowest range (20,000 ions/cm^3), they measure maximum concentration as soon as they are hit by the corona current. The ion current measuring Wilson plate, however, never registers any corona current. Instead, the Wilson plate only measures a sweep-out current, as is also displayed in another way in Fig. 5.19. The reason for this discrepancy between the ion counters and the Wilson plate, is due to the geometry of the lab setup. As is described in section 4.4, the projection of the toroid center (i.e. where the corona needle was attached) is located closer to the air ion counters, in comparison with the Wilson plate. Hence, for the ion current to reach the Wilson plate the corona region needs to be larger. In turn, this means the applied voltage must be larger. Another observation from the figure is the noisy appearance of the negative ion concentration during positive corona, and to a lesser degree the positive ion concentration during negative corona.

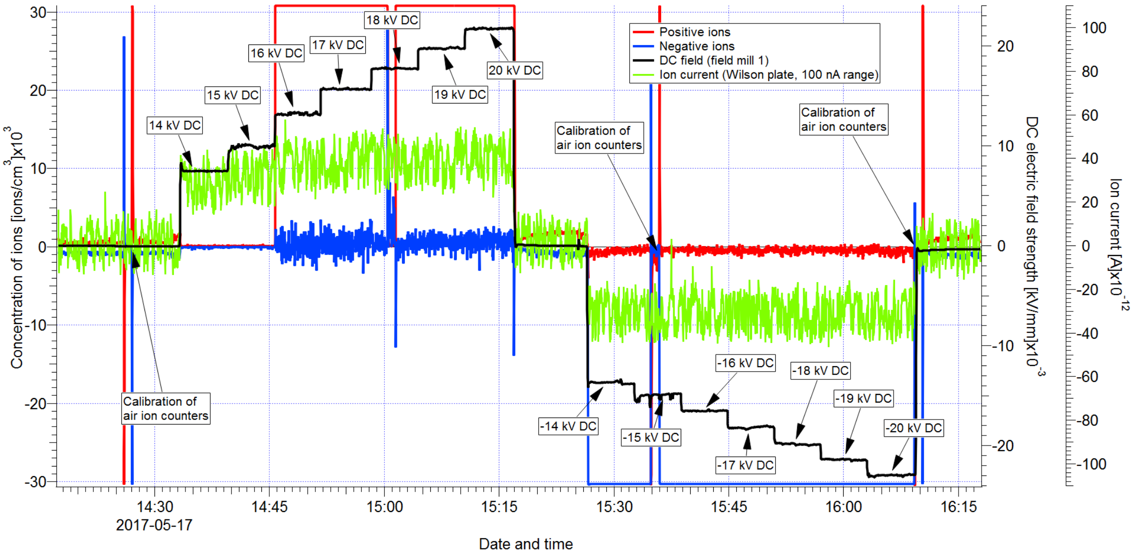

Figure 5.9: Ion concentrations, DC electric field strength, and ion current plotted versus time, from the measurement Bastu 10.

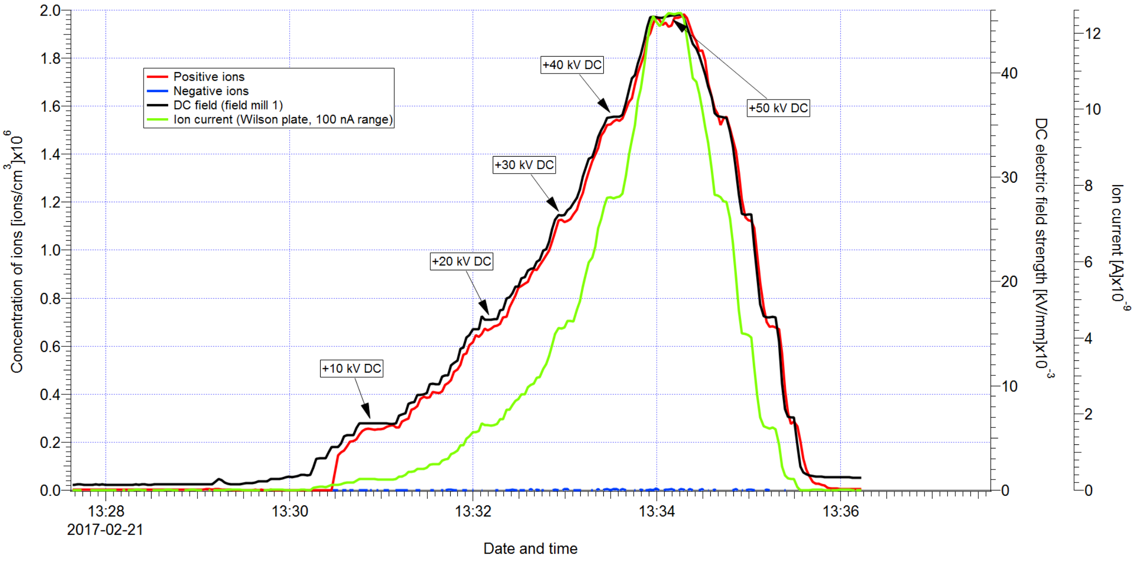

Figure 5.10: Ion concentrations, DC electric field strength, and ion current plotted versus time, from the measurement SHVH 7.

The second graph, Fig. 5.10 contains data from the measurement SHVH 7. In this measurement the range setting for the air ion counter was the largest, i.e. 2,000,000 ions/cm^3. Hence, in this graph one can observe the gradual increase in positive ion concentration as the applied voltage is increased. From the figure it can be deduced that both the positive ion concentration and the ion current follows the same staircase shape as the DC field strength. Another observation, that however is not that obvious from the figure, is that the Wilson plate registers the corona current before the air ion counters. This is in contrast to the previous graph. The explanation for this discrepancy can be found in the differences between the lab setups. The SHVH 7 measurement was performed in the small high voltage hall, where the ion box was placed in such a way the Wilson plate was almost directly under the HV electrode. Hence, for smaller voltages the corona current would be more concentrated, and reach the Wilson plate before the air ion counters.

5.7 Ion Concentrations vs. Applied Voltage

In order to compare the sweep-put effect of ions between different measurements, several graphs displaying positive and negative ion concentrations plotted versus applied voltage are presented in this section. The first graph, Fig. 5.11 contains data from measurements in small high voltage hall, with two different levels of humidity. When no voltage is applied, the concentrations are either equal, or larger for the normal humidity measurement SHVH 3. However, as voltage is applied the concentrations of both positive and negative ions are larger for the high humidity measurement SHVH 2. There can be several explanations for this phenomena. One possible explanation is ion injection due to local field enhancement provided by water vapor on e.g. the insulator surface. Another possible explanation is the effect of a small ion reservoir during high humidity levels, as described in [29]. In principle,

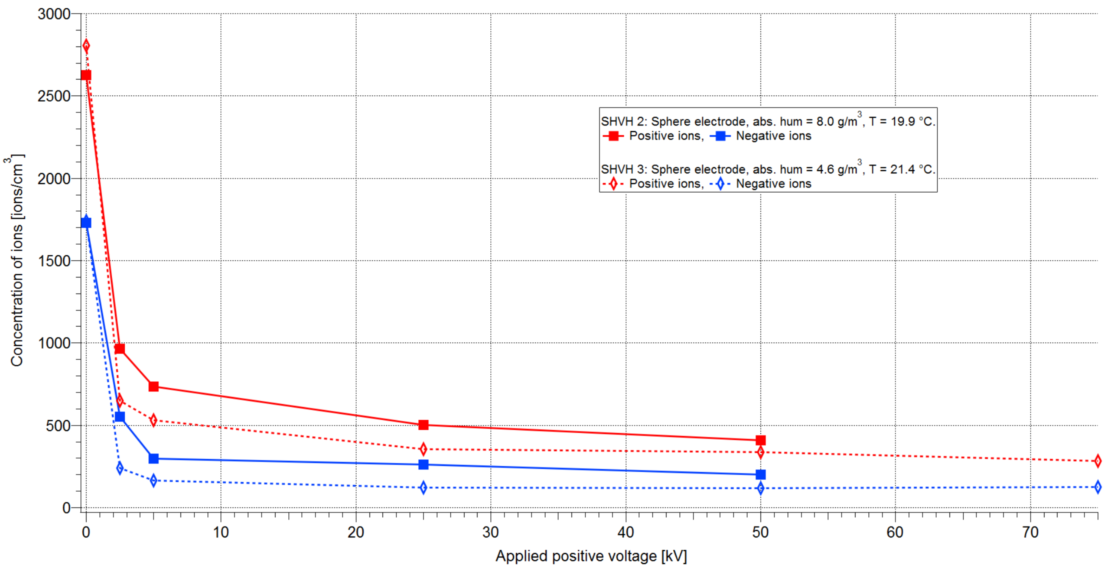

Figure 5.11: Ion concentrations plotted versus applied positive voltage, from the measurements in small high voltage hall.

this means that at high levels of humidity, larger clusters of small ions and water vapor are formed. These larger clusters have a longer life time, in comparison with the smaller and more mobile ion clusters. When a voltage is applied, however, the force of the electric field will separate the small ions and water vapor molecules again. Hence for high levels of humidity, an increase in small ion concentration during applied voltage is observed due to ion injection from the small ion reservoir.

The second graph, Fig. 5.12 contains data from measurements performed utilizing the toroid electrode in "Bastun". Three parameters are varied: fan action, humidity and temperature. In the figure positive and negative ion concentrations are plotted against applied positive voltage. The graph is altered in two ways in order to facilitate analysis. One alteration is that the vertical axis is logarithmic (base 10), and the other is the different scale on the left part of the horizontal axis (between 0 V and 1 kV). At the 0.1 kV level one can observe an increase in positive ion concentration for Bastu 7 and 12. Which is due to a non-uniform and weak electric field, i.e. the positive ions are first accelerated away from the HV electrode. Then they lose velocity, and pile up near the ground electrode. Why this effect is not observed in Bastu 8 is unknown. Another observation is that at voltages 5 kV or higher, the concentration of negative ions are larger than the corresponding concentration of positive ions. For the high humidity measurements Bastu 7 and Bastu 12, this is not that surprising considering the effect high humidity has on the negative ion concentration (see section 5.4). However, for the low humidity measurement Bastu 8, the negative ion concentration should ideally be lower than the corresponding positive ion concentration (as illustrated in Fig. 5.8). However, the differences are not large, but are magnified by the logarithmic scale on the vertical axis. From the figure one can also deduce that the largest concentration of both positive and negative ions occur for Bastu 7, i.e. the measurement with the highest humidity.

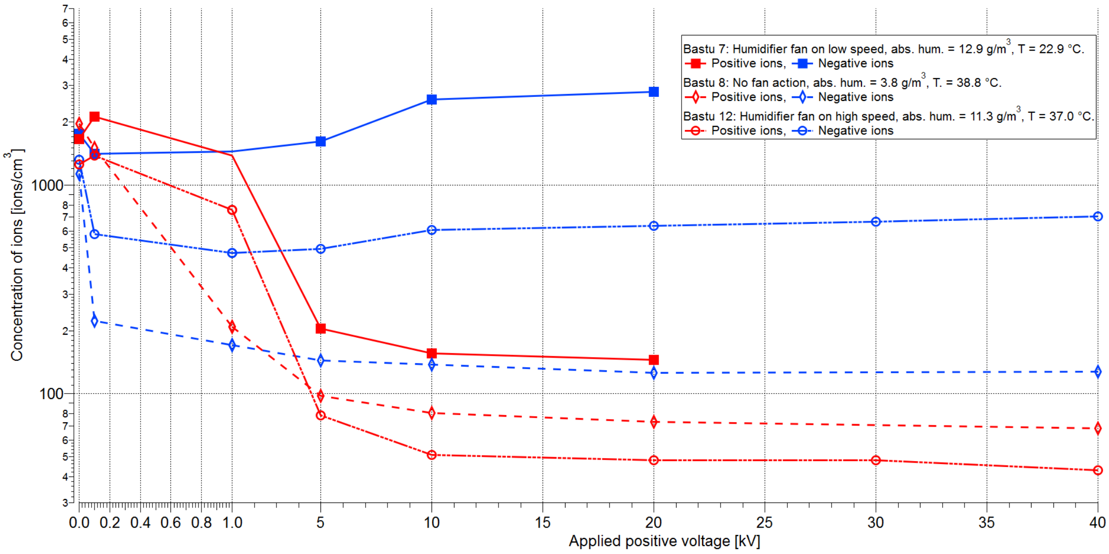

Figure 5.12: Ion concentrations plotted versus applied positive voltage, from the measurements in "Bastun".

The third graph, Fig. 5.13 contains data from the same measurements as the previous graph, but for negative voltage steps. The first thing to notice in this graph, is how the negative ion concentrations for the high humidity measurement Bastu 7 is not swept out. Instead it remains at high concentrations even at -20 kV applied voltage. Similar as for the positive voltage steps in Fig. 5.12, the highest concentration of both positive and negative ions occur for the measurement with the highest humidity, i.e. Bastu 7. Another similarity with the positive voltage steps, is the increase in negative ion concentration that occurs at -0.1 kV applied voltage. The negative concentrations are larger than the corresponding positive concentrations for each voltage step, which is expected.

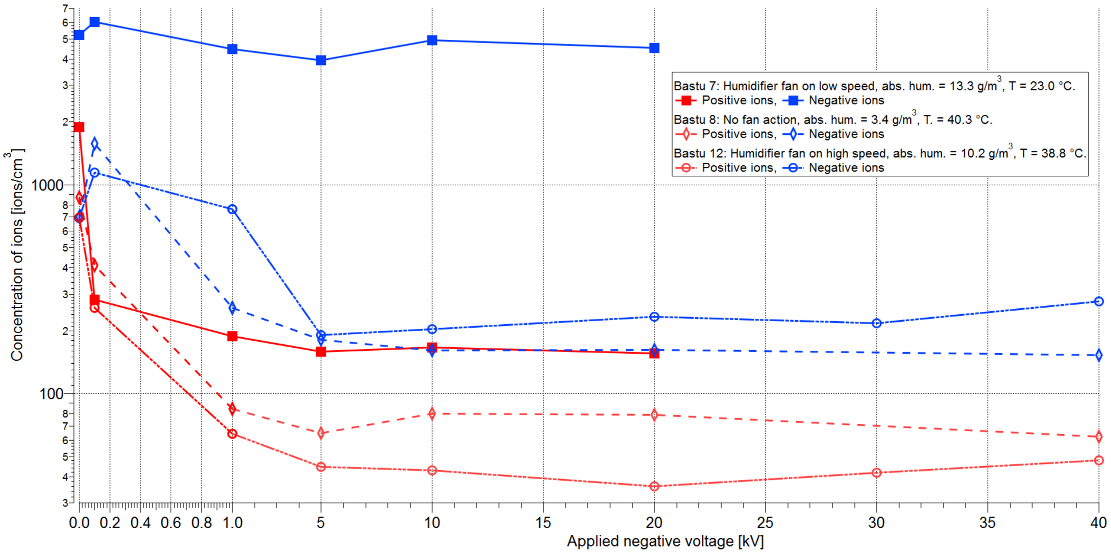

Figure 5.13: Ion concentrations plotted versus applied negative voltage, from the measurements in "Bastun".

5.8 DC Electric Field Strength vs. Applied Voltage

In order to compare the measured DC electric field strength at ground potential for different conditions, several graphs displaying DC field versus applied voltage are presented in this section. The first graph in Fig. 5.14 contains data from measurements in small high voltage hall, utilizing all the different HV electrode configurations. For the measurements performed with the sphere electrode, SHVH 2 and 3, the DC field is a linear function of the applied voltage. Furthermore, there are no noticeable differences between the two of them due to the difference in humidity. The other curves utilized setups with a corona needle, and as can be deduced from the figure they all bend at some point. The bending occurs at the same voltages the Wilson plate registered corona current, i.e. the non-linearity is probably due to corona induced space charge that disrupt the externally electric field. Another interesting observation is that the strongest field is measured in SHVH 5 for 30 kV and above. The reason for this is probably due to the long corona needle attached on the sphere electrode resulted in the most compressed equipotential lines.

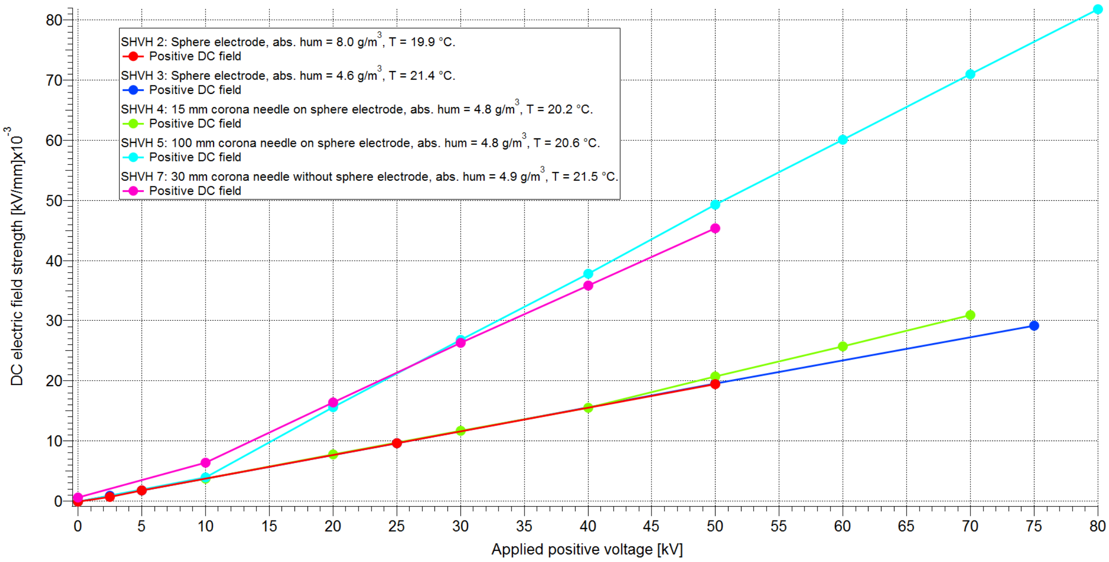

Figure 5.14: DC electric field strength plotted versus applied voltage, from the measurements in small high voltage hall.

The second graph, Fig. 5.15 contains data from measurements performed in "Bastun" utilizing the toroid HV electrode. From the figure one can deduce that all lines are straight, i.e. no space charge present. Another observation is that the negative fields strengths are generally larger, which could be related to different HV supplies (with different uncertainties) being used for generating the different voltage polarities. Furthermore, it seems that the field strength also increase with humidity.

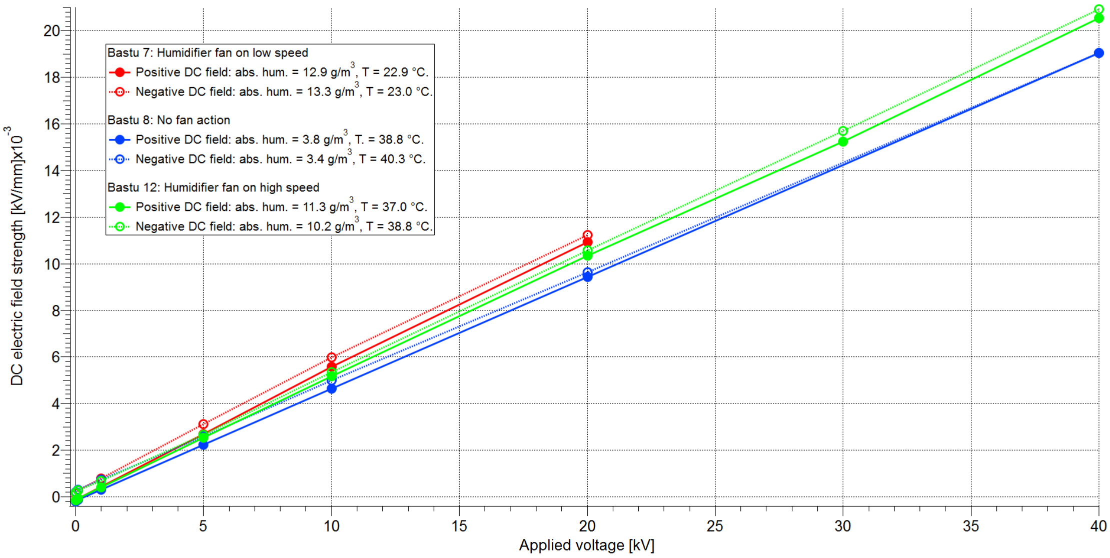

Figure 5.15: DC electric field strength plotted versus applied voltage, from the measurements in "Bastun". The toroid HV electrode without a corona needle was utilized.

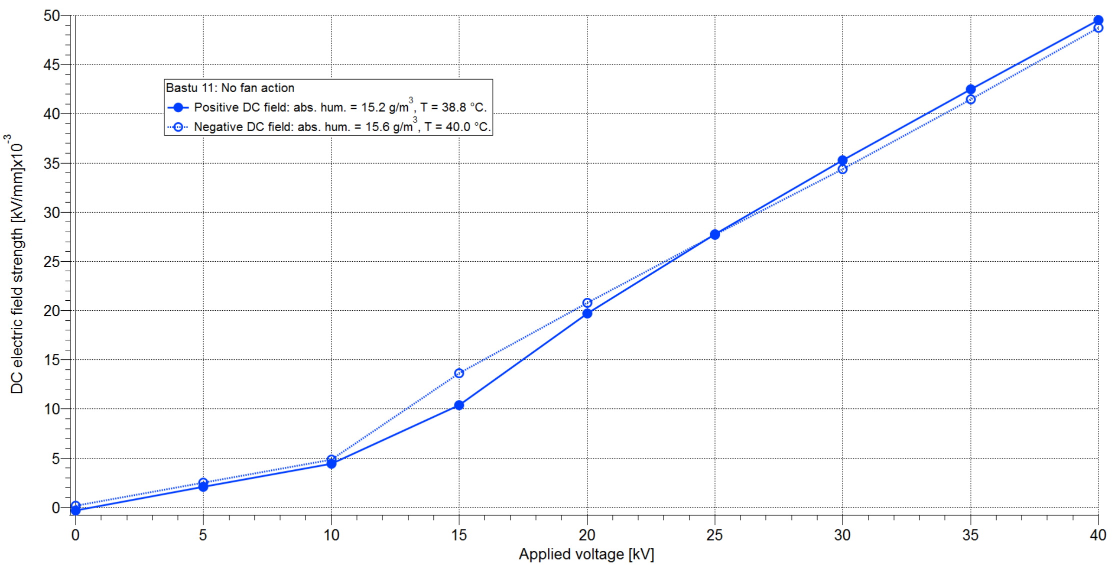

Figure 5.16: DC electric field strength plotted versus applied voltage, from the measurements in "Bastun". The setup with the corona needle attached on the toroid HV electrode was utilized.

The third graph, Fig. 5.16 contains data from measurements performed in "Bastun" utilizing the a corona needle attached on the toroid HV electrode. Similar to the plots where corona current was observed in Fig. 5.14, these plots also contain a bend. For reference, positive corona was observed with a UV camera at 14 kV applied voltage.

5.9 Ion Current vs. Applied Voltage

In order to compare the ion current measured with the Wilson plate for different conditions, several graphs displaying ion current versus applied voltage are presented in this section. The first graph in Fig. 5.17 contains data from measurements in small high voltage hall. By comparing this graph to the general current-voltage characteristic for air displayed in Fig. 2.2, one can clearly observe the ohmic region between 0 and 25 kV, and the sweep-out region above 25 kV. Since this particular Wilson plate configuration is not very sensitive, one should be careful of drawing any conclusions from these graphs, especially when the measured current are only in pA range.

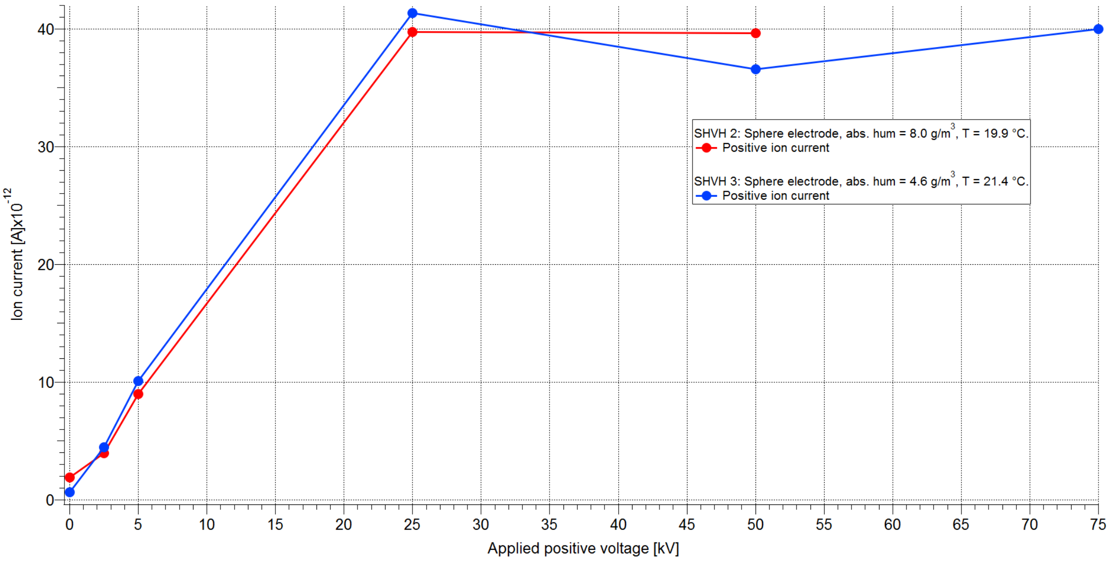

Figure 5.17: Ion current plotted versus applied voltage, from the measurements in small high voltage hall.

The second graph, Fig. 5.18 contains the same two plots as in the previous graph, but with three additional measurements also from the small high voltage hall. All three additional plots display the typical corona region (see Fig. 2.2), where the current increases significantly from the sweep-out region. Interestingly, the ion current from SHVH 5 is larger than the one from SHVH 7. This is explained by considering the electrode configuration in SHVH 5, i.e. the 100 mm corona needle attached on the sphere, which promotes a much more concentrated corona current, in comparison with SHVH 7.

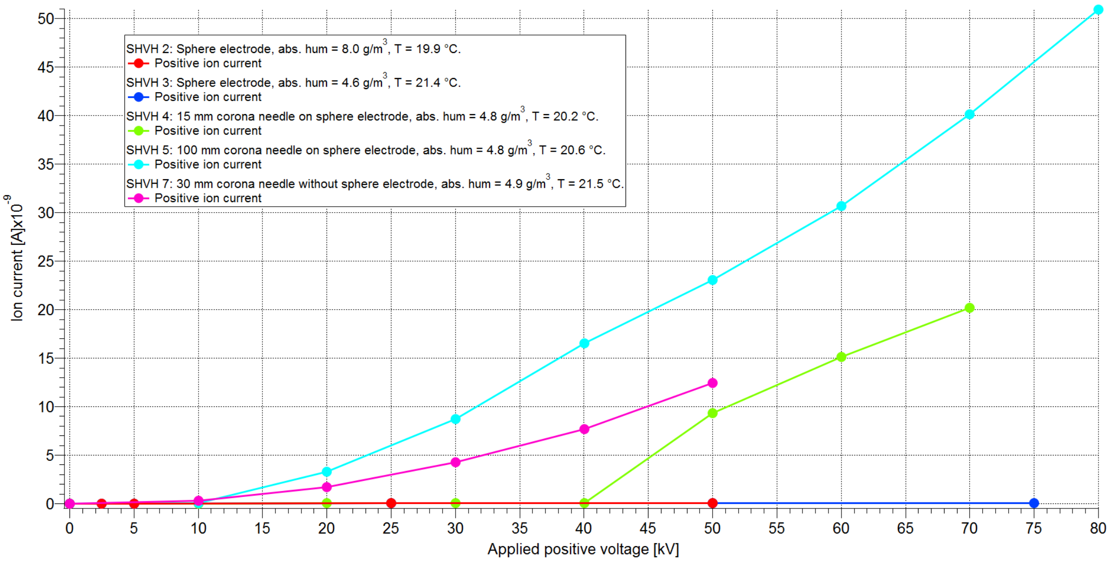

Figure 5.18: Ion current plotted versus applied voltage, from the measurements in small high voltage hall.

The third graph, Fig. 5.19 contains the data from the measurements in "Bastun" utilizing the toroid HV electrode. In the figure both positive and negative ion current are plotted against applied voltage. Positive ion current implies positive voltage, and negative ion current implies negative voltage. As with the previous graph Fig. 5.17, one can clearly observe the Ohmic region between 0 and 20 kV, and the sweep-out region between 20 and 40 kV. Another observation that can be made is that the positive ion current is generally larger than the corresponding negative ion current. But no conclusions should be drawn from this, considering that the current measurement is not very sensitive, and that different HV DC supplies (with different uncertainties) were utilized for positive and negative voltages.

Finally, the fourth graph, Fig. 5.20 contains the data from the measurements in "Bastun" utilizing the corona needle attached on the toroid HV electrode. The same characteristic regions that was observed in Fig. 5.18, can also be seen here. No noticeable difference between the two measurements is observed. However, there is a quite big difference in amplitude between the positive and negative ion current when corona is achieved at 40 kV.

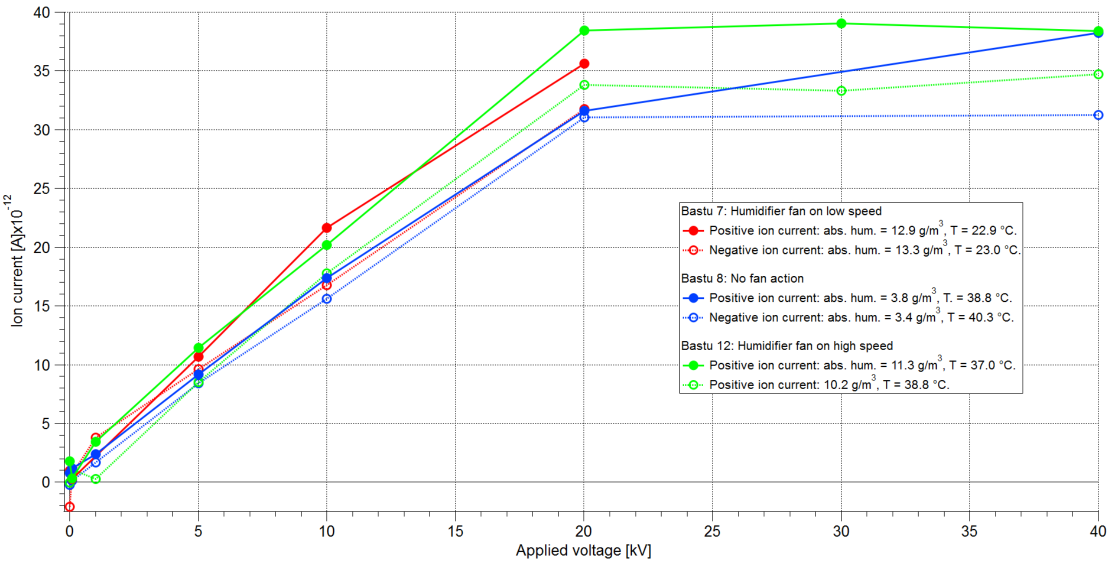

Figure 5.19: Ion current plotted versus applied voltage, from the measurements in "Bastun". The toroid HV electrode without a corona needle was utilized.

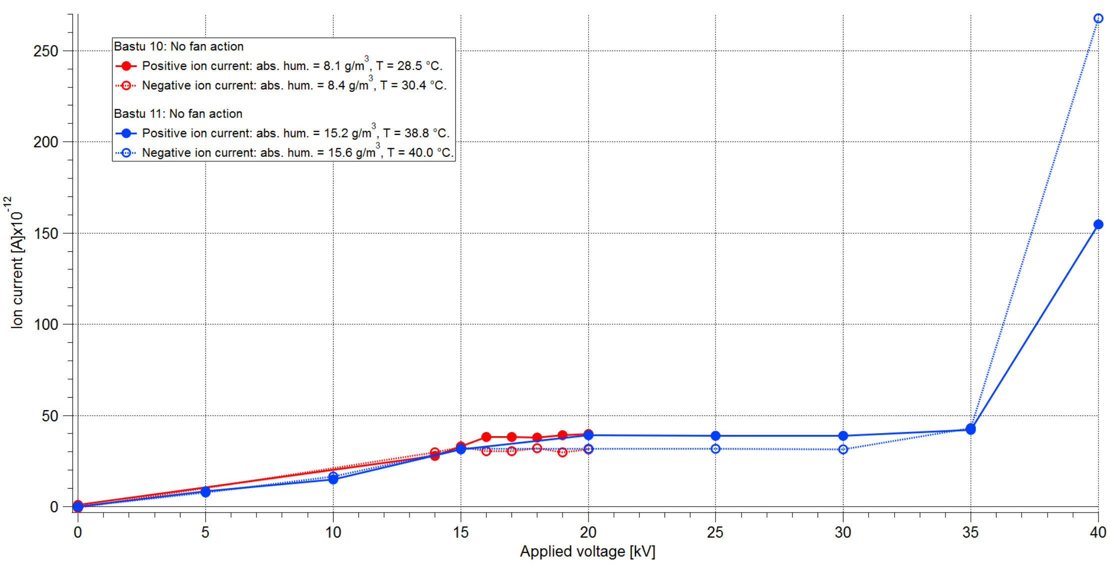

Figure 5.20: Ion current plotted versus applied voltage, from the measurements in "Bastun". The setup with the corona needle attached on the toroid HV electrode was utilized.

6

Conclusions and Future Work

6.1 Conclusions

From the indoor measurements without applied voltage one can deduce that the most important factors that affect the equilibrium ion concentrations, are concentration of radon radioactivity and air ventilation. In turn, the radon concentration is also affected by both the location and the air ventilation. It was also shown that during times when the air ventilation was on, the calculated ion concentration due to radon radioactivity tended to overestimate the values of measured ions. This suggests that the air flow caused by the air ventilation system not only affects the radon concentration, and hence ion concentrations indirectly, but perhaps also directly by increased deionization by ion-ion recombination. It could also be the case that the air ventilation alters the ratio between radon and the radon daughters, which in turn alters the ionization rate.

The ion concentrations outdoors and semi-outdoors were generally smaller in comparison with the levels indoors. This is primarily due lower levels of radon gas outdoors. In turn, this is due the open spaces and windy conditions impedes radon's ability to accumulate outdoors. By comparing the indoor, outdoor and semi-outdoor measurements it was found that the largest concentrations were measured in the basement lab. There the positive ion concentration was 4620 ions/cm^3, and the negative ions were 3820 ions/cm^3. The smallest concentration was found in Chemistry lab during daytime, where the positive ion concentration was 660 ions/cm^3, and the negative ions were 550 ions/cm^3.

From the measurements performed in the small high voltage hall both the ion sweep-out and relaxation effects were demonstrated. During sweep-out due to applied voltage, both positive and negative ion concentrations were at higher values when the humidity was higher. The measured ion concentration during corona discharges, were shown to increase with applied voltage in i similar fashion as both measured DC field strength and ion current. Furthermore, the DC field was shown to be linear with respect to applied voltage, as long as there were no corona discharges. However, during corona discharges the measured DC field displayed a bend in the earlier linear curve. The ion current measurements utilizing the Wilson plate demonstrated the three typical regions in the general current-voltage characteristics for air, i.e. ohmic, sweep-out and corona region.

The measurements in "Bastun" displayed the very large increase in negative ion concentration that occur with high levels of humidity. However, when the heating system was on simultaneously, the forced air flow effectively hindered an increase in negative ion concentration. In turn, this demonstrates that air flow is perhaps the most important parameter concerning air ion concentrations.

6.2 Future Work

There are many interesting possibilities with the ion box. One such possibility is long term outdoor measurements, that would allow for analysis of diurnal variations outdoors. However, that would require some sort of cover for the ion box to shield it from e.g. rain. Another interesting type of measurement, that was totally neglected for this thesis work, is the introduction of different types of aerosols in the measurements. Regarding high voltage measurements, it would be interesting to perform measurements with a dielectric material between the HV electrode. This would allow for air ions to accumulate as surface charges, which in turn would alter the electric field distribution. Furthermore, measurements of the air ion mobility spectrometry would be very interesting as well, e.g. to observe any changes due to humidity.

6.3 Sustainable Development and Ethics

In this paragraph sustainable development in the context of increasing voltage levels HVDC is discussed. By increasing the voltage level of HVDC transmission, the same amount of power can be transmitted using conductors of smaller size. In turn, this implies e.g. the use of less conductor material such as copper or aluminum, which might be good concerning the economical dimension. On the other hand, the increased voltage would require more insulating material such as polymer, which might be less good concerning the economical dimension. A higher voltage level could also contribute to making new installations cheaper, and perhaps providing electricity to people who previously were without it. Hence, increasing equality, which relates to the social dimension. Regarding the ecological dimension, the implementation of overhead line transmission often requires some deforestation to make room. In turn this could harm e.g. biodiversity. In this context, an increase in voltage levels for HVDC would be beneficial regarding the ecological dimension since it implies that less trees are cut down for the same amount of transmitted power.

In this paragraph point number three in IEEE Code of Ethics is discussed. It states that one should agree to “to be honest and realistic in stating claims or estimates based on available data”. Similarly, having enough measurement data facilitates the process of making realistic claims. For example, if the only equilibrium ion concentration data presented in this thesis, consisted of the Chemistry lab (during a weekend) measurement, then one could observe that the ratio between calculated ions due to radon activity and measured positive ions are unity. Hence, one could claim that radon gas is the only important parameter related to air ion concentrations. However, by performing several different measurements and comparing them, it becomes clear that although radon is a major ionization source, there are other important parameters affecting the ion concentrations as well. These include air ventilation, radiation screening, humidity and objects containing electrostatic charge.

Bibliography

[1] H.W. Beaty, D. G. Fink, *Standard Handbook for Electrical Engineers*, 16th edition, New York, USA: McGraw-Hill, 2013.

[2] C. Kim, V. K. Sood, G. Jang, S. Lim and S. Lee, *HVDC Transmission: Power Conversion Applications in Power Systems*, Singapore: Wiley-IEEE Press, 2009.

[3] ABB press releases, "ABB wins orders of over $300 million for world's first 1,100 kV UHVDC power link in China", 2016. [Online]. Available: http://www.abb.com/cawp/seitp202/f0f2535bc7672244c1257ff50025264b.aspx. Accessed: Apr. 17, 2017.

[4] N. H. Malik, A. A. Al-Arainy and M. I. Qureshi, *Electric Insulation in Power Systems*, New York, USA: CRC Press, 1997.

[5] E. Kuffel, W.S. Zaengl and J. Kuffel, *High Voltage Engineering: Fundamentals*, 2nd edition, Oxford, UK: Butterworth Heinemann, 2000.

[6] M. Schueller, R. Gremaud, C. H. Doiron and C. H. Franck, "Micro Discharges in HVDC Gas Insulated Systems", *IEEE Transactions on Dielectrics and Electrical Insulation*, vol. 22, no. 5, Oct. 2015.

[7] F. Hedenus, M. Persson and F. Sprei, *Sustainable Development: History, Definition & the Role of the Engineer*, 3rd edition, unpublished. 2016.

[8] IEEE, "IEEE Code of Ethics", 2017. [Online].
Available: http://www.ieee.org/about/corporate/governance/p7-8.html.
Accessed: Apr. 8, 2017.

[9] IEEE Std 1227-1990, "IEEE Guide for the Measurement of DC Electric-Field Strength and Ion Related Quantities".

[10] M. Saltzer, "Air DC conduction model", internal communication, 2006.

[11] National Research Council Staff, *The Earth's Electrical Environment*, Washington, D.C. USA: National Academies Press, 1986.

[12] A. Hirsikko, "On formation, growth and concentrations of air ions," Ph.D. dissertation, Department of Physics, University of Helsinki, Helsinki, Finland, 2011.

[13] H. Volland, *Physics and Chemistry in Space vol. 11: Atmospheric Electrodynamics*, Berlin-Heidelberg, Germany: Springer-Verlag, 1984.

[14] Michael F. L'Annunziata, *Handbook of Radioactivity Analysis*, San Diego, USA: Academic Press, 1998.

[15] J. S. Duval, L. E. Fukumoto, J. M. Fukumoto, and S. L. Snyder, "Geology and Indoor Radon in Schools of the Palos Verdes Peninsula Unified School District, Palos Verdes Peninsula, California," U.S. Geological Survey, U.S. Department of Interior, Open-File Report 2004-1050.

[16] Wang et al., “The AME2016 atomic mass evaluation (II)”, *Chinese Physics C*, vol. 41, no. 3, Mar. 2017, [Online].
Available: http://amdc.impcas.ac.cn/ame2016/ame16-intro.html.
Accessed: Apr. 20, 2017.

[17] P. Kolarz, M. Gaisberger, P. Madl, W. Hofmann, M.Ritter and A. Hartl, “Characterization of ions at Alpine waterfalls”, *Atmospheric Chemistry and Physics*, 24 Apr. 2012.

[18] U. Hõrrak, “Air Ion Mobility Spectrum at a Rural Area,” Ph.D. dissertation, Department of Physics, University of Tartu, Tartu, Estonie, 2001.

[19] D. K. Cheng, *Field and Wave Electromagnetics*, second edition, Harlow, UK: Pearson Education Limited, 2014.

[20] *Manual MP MOTION SENSOR ‘NaPiOn’*, 2012 [Online]. Available: http://www3.panasonic.biz/ac/e_download/control/sensor/human/catalog/bltn_eng_mp.pdf. Accessed: Mars 22. 2017.

[21] *HS-135 Air pollution sensor specification*, n.d. [Online]. Available: https://ciiva.com/part/hs-135-8612495. Accessed: Apr. 25. 2017.

[22] *GAMMA-SCOUT Manual*, 2015 [Online]. Available: https://www.gamma-scout.com/Download/Manual-EN.pdf. Accessed: January 23. 2017.

[23] *Mätprincipen i R1*, n.d. [Online].
Available: http://www.radonelektronik.se/R1.htm. Accessed: Apr. 25. 2017.

[24] *Air Ion Counter, Model AIC Full Length Instructions*, 2014 [Online].
Available: https://www.trifield.com/content/air-ion-counter/.
Accessed: February 6. 2017.

[25] B. Lee, AlphaLab, Inc., private communication, Feb. 2017.

[26] Universal Plan Co., Ltd., Ion Trading, “Air Ion Counter IC-1000,” 2017. [Online]. Available: http://www.n-ion.com/e/product/ion-counter/ic-1000.html. Accessed: February 20. 2017.

[27] K. L. Aplin, “Instrumentation for atmospheric ion measurements,” Ph.D. dissertation, Department of Meteorology, The University of Reading, Reading, United Kingdom, 2000.

[28] *Manual electro field meter EFM 113B*, 2011 [Online]. Available: http://www.kleinwaechtergmbh.de/cms/front_content.php?idcat=113.
Accessed: Mars 12. 2017.

[29] P. Ortéga, R. Díaz, F. Heilbronner, and F. Rühling, “Influence of negative ions on the humidity effect on the first corona inception”, *Journal of Physics D: Applied Physics*, vol. 40, Nov. 2007.

A

Appendix 1

A.1 Environmental Conditions for the Equilibrium Measurements

In this section environmental conditions for the equilibrium measurements described in Section 4.1 and 4.2 are presented.

Table A.1: Environmental conditions for the indoor measurements presented in Section 4.1.

Parameter	**Preparations lab (during a weekend)**	**Chemistry lab (during a weekend)**	**Basement lab**	**Conference room "Spänningen"**
Relative humidity [%]	17.8	21.0	29.6	25.7
Absolute humidity [g/m^3]	3.4	3.5	4.9	5.1
Ambient temperature [°C]	21.9	23.4	21.9	22.4
Air pressure [kPa]	99.8	101.7	101.2	101.4
Gamma radiation [µSv/h]	0.198	0.205	0.201	0.173

Table A.2: Environmental conditions for the outdoor and semi-outdoor measurements presented in Section 4.2.

Parameter	**Outdoors 1**	**Outdoors 2**	**Semi-outdoors 1**	**Semi-outdoors 2**
Relative humidity [%]	22.4	14.2	55.1	49.6
Absolute humidity [g/m^3]	3.7	4.2	3.0	3.6
Ambient temperature [°C]	16.9	30.7	1.6	6.6
Air pressure [kPa]	100.1	103.3	101.3	102.0
Gamma radiation [µSv/h]	0.169	0.441	0.235	0.411

A.2 Measured and Calculated Steady-state Values

In Table A.3 several measured and calculated quantities are presented. The calculations are performed as described in 5.2. The measurement uncertainties are calculated by taken into consideration the accuracy of each device, which are ±25 % for the air ion counters and ±10-20 % (depending on both the measured average and measurement duration) for the R1 Radon Monitor. The accuracy of the Agilent DAQ unit is negligible in comparison with the accuracy of the air ion counters, and is hence neglected. Furthermore, the uncertainties in the calculated values, are determined by taking into consideration the propagation of uncertainty through the expressions utilized.

Table A.3: Measured and calculated steady-state values from indoor measurements described in Section 4.1.

	Preparations lab (during a weekend)	**Chemistry lab (during a weekend)**
Measured radon radioactivity concentration [Bq/m^3]	52.73 ± 5.27	54.17 ± 5.41
Measured positive ion concentration [ions/cm^3]	2918 ± 730	2380 ± 595
Measured negative ion concentration [ions/cm^3]	2316 ± 579	2187 ± 547
Calculated ion concentration [ions/cm^3]	2348 ± 117	2380 ± 119
Calculated conductivity [S/m], using measured ion concentrations	$(1.34 \pm 0.24)\cdot 10^{-13}$	$(1.17 \pm 0.21)\cdot 10^{-13}$
Calculated conductivity [S/m], using measured radon radioactivity	$(1.20 \pm 0.06)\cdot 10^{-13}$	$(1.22 \pm 0.06)\cdot 10^{-13}$
	Basement lab	**Conference room "Spänningen"**
Measured radon radioactivity concentration [Bq/m^3]	167.41 ± 16.74	82.97 ± 8.30
Measured positive ion concentration [ions/cm^3]	4618 ± 1155	4159 ± 1039
Measured negative ion concentration [ions/cm^3]	3820 ± 955	3293 ± 823
Calculated ion concentration [ions/cm^3]	4184 ± 209	2945 ± 147
Calculated conductivity [S/m], using measured ion concentrations	$(2.16 \pm 0.38)\cdot 10^{-13}$	$(1.91 \pm 0.34)\cdot 10^{-13}$
Calculated conductivity [S/m], using measured radon radioactivity	$(2.14 \pm 0.11)\cdot 10^{-13}$	$(1.51 \pm 0.08)\cdot 10^{-13}$

Table A.4: Measured and calculated steady-state values from the outdoor and semi-outdoor measurements described in Section 4.2.

	Outdoors 1	**Outdoors 2**
Measured radon radioactivity concentration [Bq/m^3]	13.5 ± 2.7	12.33 ± 2.47
Measured positive ion concentration [ions/cm^3]	1491 ± 373	1499 ± 375
Measured negative ion concentration [ions/cm^3]	1203 ± 301	1357 ± 339
Calculated ion concentration [ions/cm^3]	1188 ± 59	1136 ± 57
Calculated conductivity [S/m], using measured ion concentrations	$(6.91 \pm 1.23) \cdot 10^{-14}$	$(7.32 \pm 1.30) \cdot 10^{-14}$
Calculated conductivity [S/m], using measured radon radioactivity	$(6.09 \pm 0.31) \cdot 10^{-14}$	$(5.82 \pm 0.29) \cdot 10^{-14}$
	Semi-outdoors 1	**Semi-outdoors 2**
Measured radon radioactivity concentration [Bq/m^3]	14.9 ± 1.5	9.5 ± 1.0
Measured positive ion concentration [ions/cm^3]	2624 ± 656	1884 ± 471
Measured negative ion concentration [ions/cm^3]	2214 ± 553	1609 ± 402
Calculated ion concentration [ions/cm^3]	1247 ± 62	997 ± 50
Calculated conductivity [S/m], using measured ion concentrations	$(1.24 \pm 0.22) \cdot 10^{-13}$	$(8.95 \pm 1.59) \cdot 10^{-14}$
Calculated conductivity [S/m], using measured radon radioactivity	$(6.39 \pm 0.32) \cdot 10^{-14}$	$(5.11 \pm 0.26) \cdot 10^{-14}$

A.3 Measured Ion and Radon Radioactivity Concentrations

In this section additional graphs for the indoor, outdoor and semi-outdoor measurements described in Section 4.1 and 4.2 are presented.

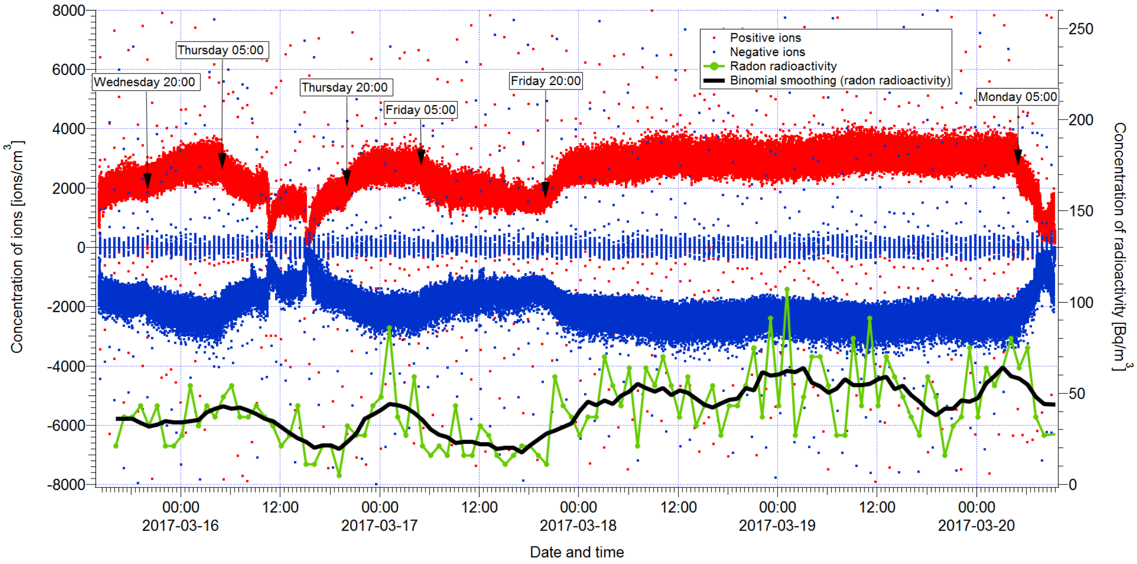

Figure A.1: Concentrations of ions and radon radioactivity plotted versus time, from the measurement in Preparations lab.

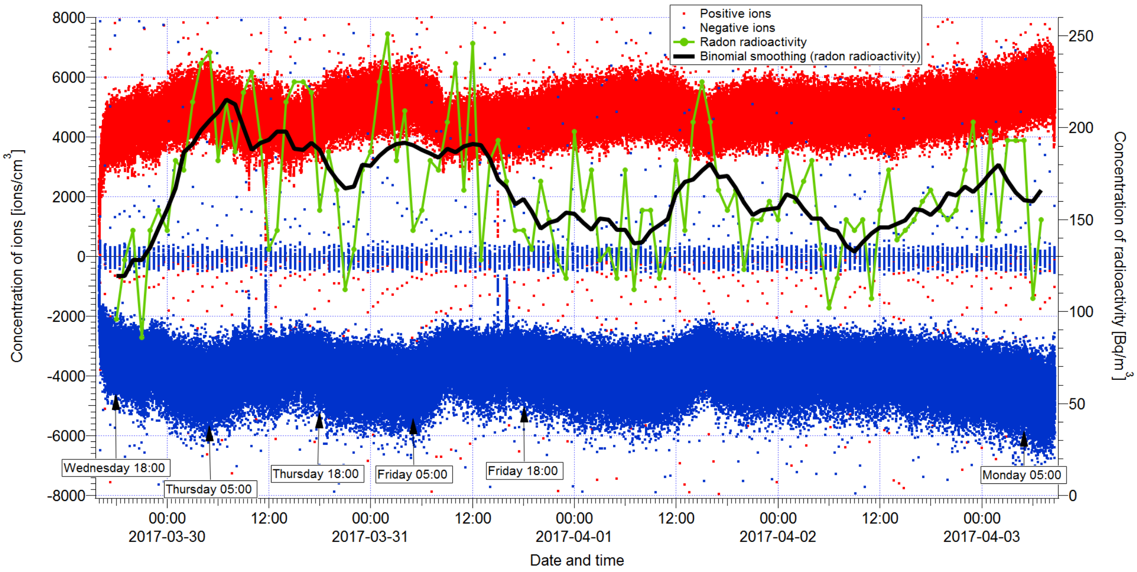

Figure A.2: Concentrations of ions and radon radioactivity plotted versus time, from the measurement in the basement lab.

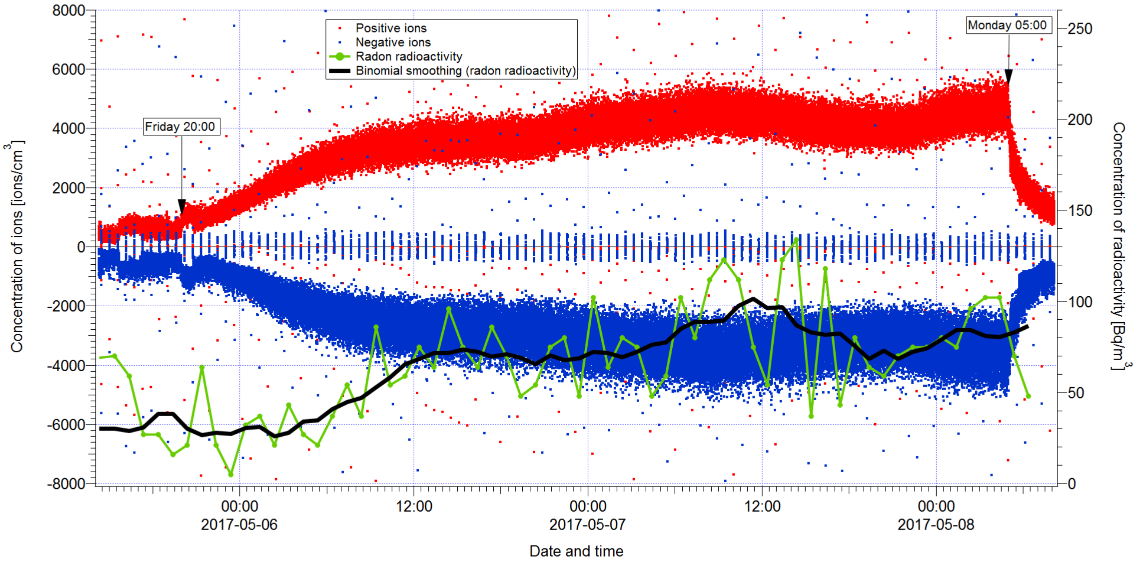

Figure A.3: Concentrations of ions and radon radioactivity plotted versus time, from the measurement in the conference room "Spänningen".

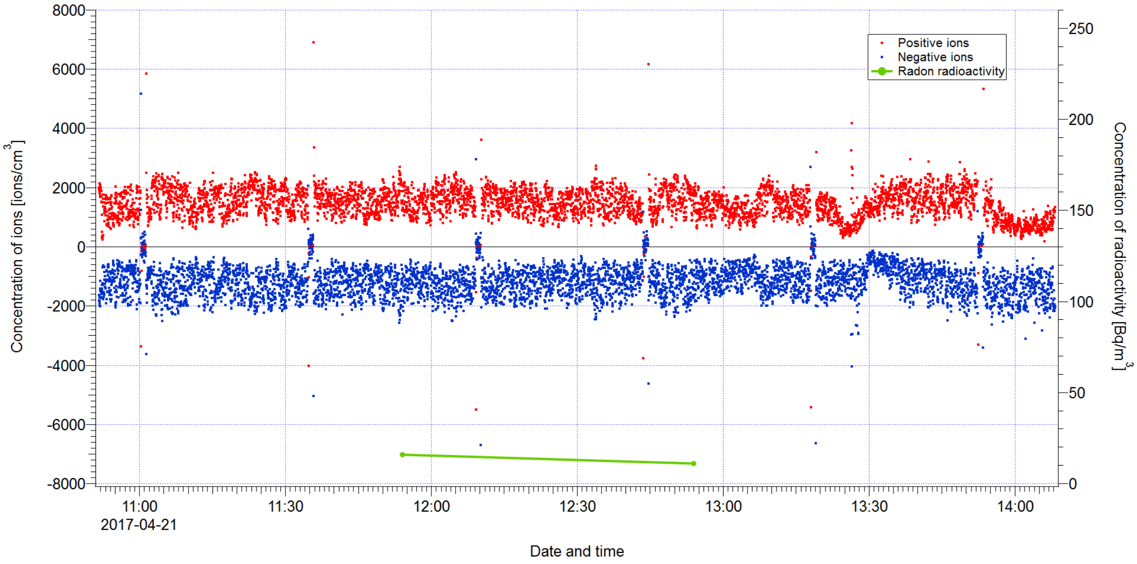

Figure A.4: Concentrations of ions and radon radioactivity plotted versus time, from the measurement Outdoors 1.

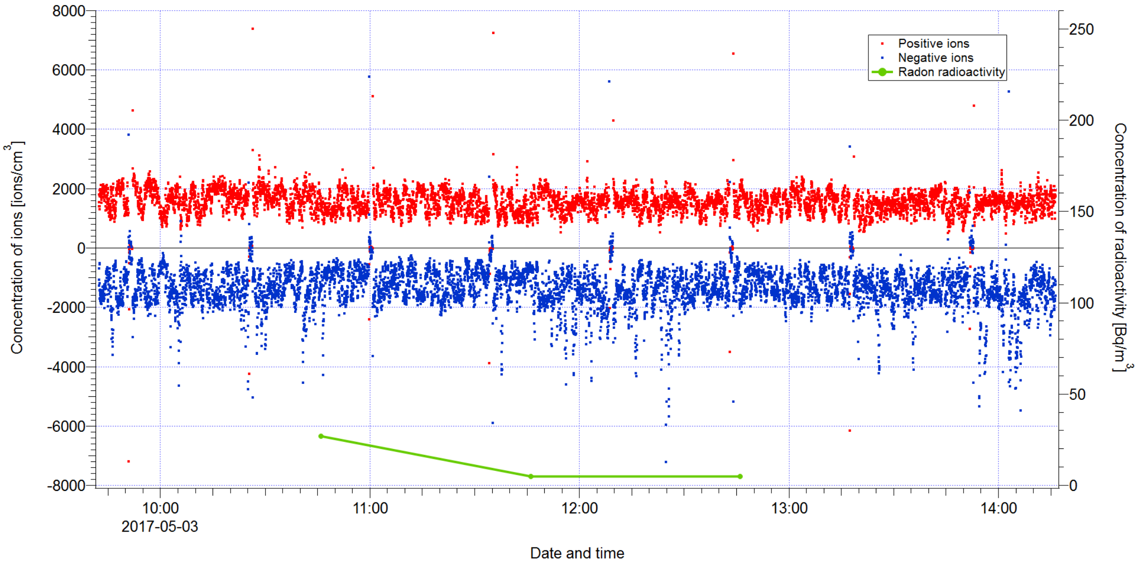

Figure A.5: Concentrations of ions and radon radioactivity plotted versus time, from the measurement Outdoors 2.

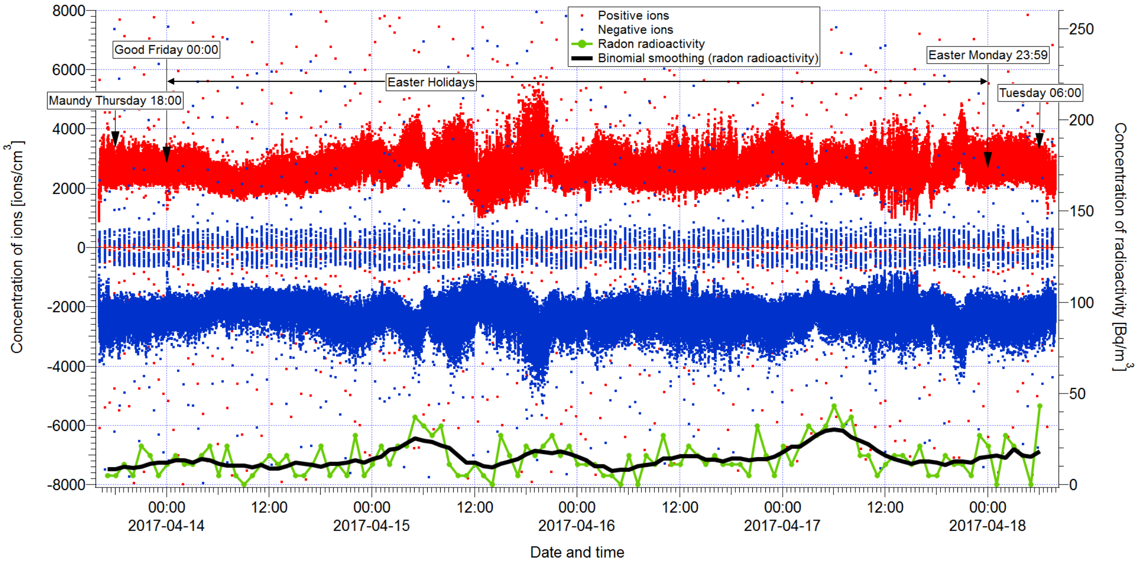

Figure A.6: Concentrations of ions and radon radioactivity plotted versus time, from the measurement Semi-outdoors 1.

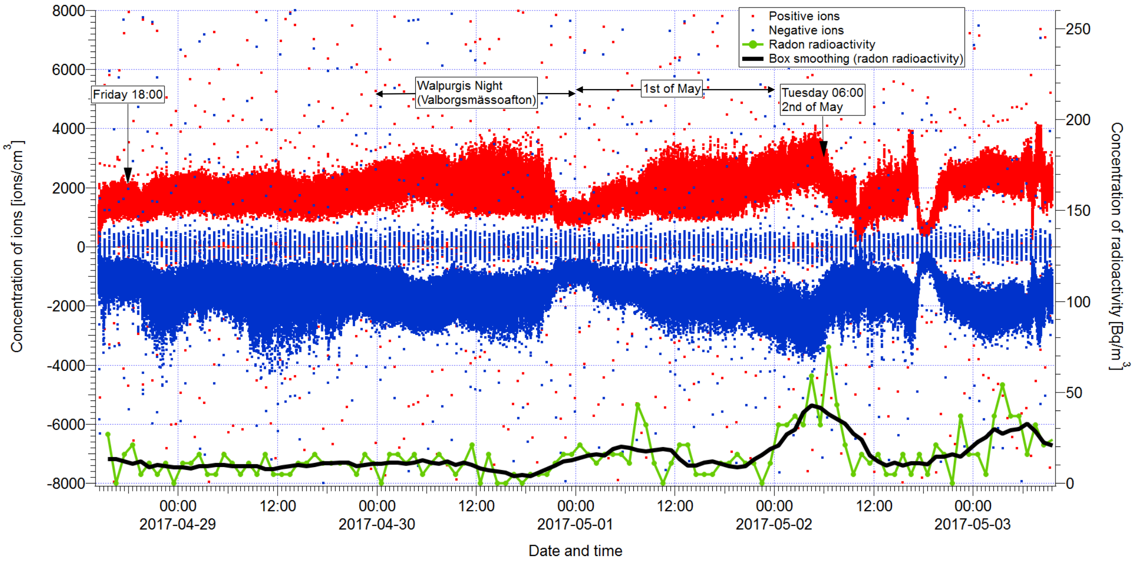

Figure A.7: Concentrations of ions and radon radioactivity plotted versus time, from the measurement Semi-outdoors 2.